Switching behavior of the superconducting $Ni_{80}Fe_{20}/Nb/Ni_{80}Fe_{20}$ spin valve

J.M. van der Knaap

Leiden, June 21, 2007

Contents

Chapter 1

Introduction

The contact between a superconductor (S) and a ferromagnet (F) leads to a non-trivial proximity effect due to the exchange field of the ferromagnet. This leads to a non-trivial effect in the electronic ground state. A particular interesting system is the superconducting spin valve, which consists of a superconducting layer sandwiched between two ferromagnet layers. The ground state of a ferromagnet has the spins of all electrons aligned. The ground state of a superconductor has its electrons bound in Cooper pairs consisting of two electrons with opposite momenta and spins. Thus the two materials have different types of order. They influence each other via the *proximity effect*. Cooper pairs can leak from the superconductor into the ferromagnet by Andreev reflection, causing superconducting properties in the ferromagnet and a decrease of the superconducting properties in the superconductor. The Andreev reflection will be described in section 4.1.

In an F/S/F spin valve it is possible to control the superconductivity in the S layer by manipulating the relative magnetic orientation of the F layers. It was predicted theoretically by Tagirov [1] and Buzdin [2] that, if a *weak* ferromagnet is used, a parallel (P) configuration of the F layers gives a larger suppression of the T_c (critical temperature) of the superconductor than an antiparallel (AP) orientation. They assumed homogeneously magnetized F layers, without domain walls or other defects. In practice such a sample is difficult to fabricate, it will always contain some domains and domain walls. The presence of domain walls will influence the superconductor; they cause local inhomogeneity because the direction of the magnetization at both sides of the domain wall is different. This leads to less suppression of the superconductivity. But a domain wall also causes flux to penetrate the superconductor which can suppress the superconductivity more.

Gu et al.[3] provided experimental evidence which showed that $T_c(AP)>T_c(P)$ for an F/S/F structure with weak ferromagnets, as expected from theory. For strong ferromagnets no theory is available. Rusanov et al. showed that the strong ferromagnet they have used yield the opposite effect ($T_c(AP)<T_c(P)$)[4].

In this report measurements are presented on F/S/F structures where F is in this case $Ni_{80}Fe_{20}$ (Py) and Nb was used as superconductor. Py is a strong ferromagnet, E_{ex} is approximately 270 meV and it is 45% spin polarized [5]. The effects are only visible if the S layer is thin, in the order of the superconducting coherence length. We used thicknesses from 15 to 70 nm. To control the P and AP states we made use of the thickness dependence of the coercive field of the Py layers. The used Py thicknesses were 20 nm and 50 nm, Py layers with these thicknesses behave still like bulk samples and therefore we expect that 20 and 50 nm layers have the same properties except for the coercive field. The samples were structured in strips to exclude the effects of domain walls as much as possible. The width of the sample strip is $\sim$1 μm to be nearly single domain. The length is $\sim$40 μm. Resistance was measured as function of temperature (RT) in different fields, applied field (RH) at different temperatures and current (IV) at different fields and temperatures.

Outline of the report Chapter 2 describes the theory involving superconductivity. Chapter 3 is used for the theory needed for the description of ferromagnetism and chapter 4 for the proximity effect in S/N, S/F and F/S/F structures. Chapter 5 contains the experimental methods and the results are presented in chapter 6. The conclusion will be drawn in chapter 7. The details of sample preparation and sample dimensions are given in appendices A and B respectively.

Chapter 2

Superconductivity

In 1935, before the actual microscopic mechanism of superconductivity was discovered, the brothers F. and H. London proposed two phenomenological equations similar to the Maxwell equations to describe the behavior of a superconductor [6]. They are like the Maxwell equations in the sense that they describe the microscopic electric $\vec{E}$ and magnetic $\vec{h}$ fields inside the superconductor. The equations are:

$$\vec{E} = \frac{\partial}{\partial t}(\Lambda \vec{J}_s) \tag{2.1}$$

$$\vec{h} = -\nabla \times (\Lambda \vec{J}_s) \tag{2.2}$$

where

$$\Lambda = \mu_0 \lambda^2 = \frac{m}{n_s e^2} \tag{2.3}$$

with Λ a phenomenological parameter, λ the *penetration depth* (to be explained below), n_s the density of superconducting electrons, m the electron mass and e its charge. $\vec{J}_s$ is the supercurrent density. It was thought that not all electrons are superconducting, but only a certain fraction. This fraction would vary continuously from zero at T_c, the transition temperature, to a limiting value of the order of n, the density of conduction electrons, far below T_c. The first London equation describes perfect conductivity. The electric field is accelerating the electrons continuously instead of sustaining their velocity against resistance. The second equation describes the screening of the magnetic field. It implies that a magnetic field is exponentially screened from the interior of the superconductor with a characteristic length scale λ, the penetration depth. The temperature dependence of λ is empirically described by

$$\lambda(T) \approx \lambda(0)(1 - (T/T_c)^4)^{-1/2} \tag{2.4}$$

with

$$\lambda(0) = \left(\frac{m}{\mu_0 n_s e^2}\right)^{1/2} \tag{2.5}$$

To improve this, a non-local generalization was introduced. In analogy with the idea of non-locality in electrodynamics (the current at a point depends on the electric field around that point) Pippard introduced another characteristic length scale ξ_0, the *coherence length*. The coherence length takes care of the fact that a superconducting wavefunction is not local. The definition of the coherence length was

$$\xi_0 = a\frac{\hbar v_F}{k_B T_c} \tag{2.6}$$

with v_F the Fermi velocity and a a numerical constant of order unity. The exact value of a is found by BCS theory to be 0.18.
The ability of a supercurrent to screen magnetic fields is finite and superconductivity is destroyed above a critical field H_c. If a field higher than H_c is applied, the sample is not superconducting anymore. H_c is also dependent on temperature. Exactly at T_c, H_c is in fact 0 and it reaches a finite field at 0 K. Also I_c exists, the critical (depairing) current. Above a certain current the superconductivity is destroyed and normal resistance appears.

2.1 BCS theory

In 1957 Bardeen,Cooper and Schrieffer (BCS) published their microscopic theory of superconductivity. They continued the ideas of Cooper that any attractive interaction between electrons can lead to superconducting properties. Even a weak attractive interaction can cause electrons to form bound pairs (*Cooper pairs*). Only a small amount of electrons in the superconductor are bound in pairs, these are responsible for the superconductivity, short-circuiting the remaining electrons which still have a finite resistance.

2.1.1 Cooper pairs

In 1956 Cooper showed that a Fermi sea is not stable against the formation of at least one bound pair of electrons. The electrons are bound by an attractive interaction, which can be very weak, every net attractive interaction will form a pair. Cooper considered a entirely filled Fermi sea at $T = 0$ and added two more electrons. He considered what energy is needed to do this. In a normal free electron model the energy of the two electrons would be higher than $2E_F$, the Fermi energy of two electrons. If the energy is lower than $2E_F$ the system can save energy by binding its electrons in pairs. If a net attraction exists, electron pairs with $E < 2E_F$ appear. The density of these bound states strongly depends on the total momentum $\vec{k}$ of the pair with a maximum when $\vec{k} = 0$. The energy of the pair is now

$$E \approx 2E_F - 2\hbar\omega_c e^{-2/N(0)V} \tag{2.7}$$

where $\hbar\omega_c$ is a cut off energy, $N(0)$ is the density of states at the Fermi level for electrons of one spin orientation and V is the interaction potential. Assumed is that the weak-coupling approximation is applicable, i.e. $N(0)V \ll 1$. Equation 2.7 says that the energy of the pair is lower than the Fermi energy if there is an attractive interaction, no matter how weak it is. This means that the system can lower its energy by binding electrons in Cooper pairs and the Fermi sea becomes unstable.
The origin of the attractive potential is not specified and can in principle be every attractive interaction. In conventional superconductors it is the electron-phonon interaction. This is confirmed experimentally by the discovery of the *isotope effect*. T_c and H_c are proportional to $M^{-1/2}$ for isotopes of the same element (M is the isotopic mass).

2.1.2 BCS ground state

BCS continued on this idea by considering how the ground state of such a system with attractive interactions between the electrons should look like. The BCS ground state is most easily expressed using the language of second quantization. Occupied states are specified by the use of creation operators ($c^\dagger_{\mathbf{k}\uparrow}$). Annihilation operators ($c_{\mathbf{k}\uparrow}$) are introduced to empty the state. As Hamiltonian we use the so-called pairing Hamiltonian or reduced Hamiltonian:

$$H = \sum_{\mathbf{k}\sigma} \xi_{\mathbf{k}} n_{\mathbf{k}\sigma} + \sum_{\mathbf{kl}} V_{\mathbf{kl}} c^\dagger_{\mathbf{k}\uparrow} c^\dagger_{-\mathbf{k}\downarrow} c_{-\mathbf{l}\downarrow} c_{\mathbf{l}\uparrow} \tag{2.8}$$

where only the simplest interactions are included that lead to superconductivity, omitting many others. Here σ is used for the spin index ($\uparrow$ or $\downarrow$) and ξ is the energy measured from the Fermi energy. $n_{\mathbf{k}\sigma}$ is the particle number operator. The first term in the Hamiltonian describes the kinetic energy of the electrons. The second term is the pairing interaction, as it describes how two electrons with momentum $\vec{l}$ and $-\vec{l}$ are scattered into states with momentum $\vec{k}$ and $-\vec{k}$. Because of the large number of particles involved it is convenient to decompose the pair operators in an average and a fluctuation:

$$c_{-\mathbf{k}\downarrow} c_{\mathbf{k}\uparrow} = b_{\mathbf{k}} + (c_{-\mathbf{k}\downarrow} c_{\mathbf{k}\uparrow} - b_{\mathbf{k}}) \tag{2.9}$$

with

$$b_{\mathbf{k}} = \langle c_{-\mathbf{k}\downarrow} c_{\mathbf{k}\uparrow} \rangle_{av} \tag{2.10}$$

The fluctuation can be assumed to be very small. Equation 2.9 can be substituted in equation 2.8 and higher order terms in the fluctuation will be neglected because they are expected to be very small since the fluctuation is already small. We obtain the following:

$$H = \sum_{\mathbf{k}\sigma} \xi_{\mathbf{k}} c^{\dagger}_{\mathbf{k}\sigma} c_{\mathbf{k}\sigma} + \sum_{\mathbf{kl}} V_{\mathbf{kl}} (c^{\dagger}_{\mathbf{k}\uparrow} c^{\dagger}_{-\mathbf{k}\downarrow} b_{\mathbf{l}} + b^{\dagger}_{\mathbf{k}} c_{-\mathbf{l}\downarrow} c_{\mathbf{l}\uparrow} - b^{\dagger}_{\mathbf{k}} b_{\mathbf{l}}) \tag{2.11}$$

Defining:

$$\Delta_{\mathbf{k}} = -\sum_{\mathbf{l}} V_{\mathbf{kl}} b_{\mathbf{l}} = -\sum_{\mathbf{l}} V_{\mathbf{kl}} \langle c_{-\mathbf{l}\downarrow} c_{\mathbf{l}\uparrow} \rangle \tag{2.12}$$

and substituting this in equation 2.11 results in the following Hamiltonian:

$$H = \sum_{\mathbf{k}\sigma} \xi_{\mathbf{k}} c^{\dagger}_{\mathbf{k}\sigma} c_{\mathbf{k}\sigma} - \sum_{\mathbf{k}} (\Delta_{\mathbf{k}} c^{\dagger}_{\mathbf{k}\uparrow} c^{\dagger}_{-\mathbf{k}\downarrow} + \Delta^{\dagger}_{\mathbf{k}} c_{-\mathbf{k}\downarrow} c_{\mathbf{k}\uparrow} - \Delta_{\mathbf{k}} b^{\dagger}_{\mathbf{k}}) \tag{2.13}$$

Δ is an important parameter. It is called the superconducting *order parameter* and is a measure for the energy gap between the Cooper pairs and their excitations (*quasiparticles*). Δ is proportional to the number of superconducting electrons and is thus zero above T_c. Below T_c it has a finite value and reaches its maximum at T=0. Therefore it can be used as an order parameter.
Sofar everything was done at T=0. At finite temperatures we have to add excitations. But BCS were using single particle operators and the elementary excitations of the system are pairs of electrons with opposite momentum or, equivalently, electron/hole pairs with the same momentum. To make the theory more useful at finite temperatures, new operators $\gamma_{\mathbf{k}}$ and $\gamma^{\dagger}_{\mathbf{k}}$ can be introduced by a Bogoliubov transformation. These new operators are linear combinations of the old ones and directly create and annihilate these elementary excitations. The operators are defined through the relations:

$$c_{\mathbf{k}\uparrow} = u^{\dagger}_{\mathbf{k}} \gamma_{\mathbf{k}0} + v_{\mathbf{k}} \gamma^{\dagger}_{\mathbf{k}1} \tag{2.14}$$

$$c^{\dagger}_{-\mathbf{k}\downarrow} = -v^{\dagger}_{\mathbf{k}} \gamma_{\mathbf{k}0} + u_{\mathbf{k}} \gamma^{\dagger}_{\mathbf{k}1} \tag{2.15}$$

with $u_{\mathbf{k}}$ and $v_{\mathbf{k}}$ satisfying

$$|u_{\mathbf{k}}|^2 + |v_{\mathbf{k}}|^2 = 1 \tag{2.16}$$

Using this operators the Hamiltonian can be diagonalized. If these operators are substituted in equation 2.13, $u_{\mathbf{k}}$ and $v_{\mathbf{k}}$ have to be chosen such that the undesired terms vanish. The Hamiltonian is diagonalized if the following condition is satisfied:

$$|v_{\mathbf{k}}|^2 = 1 - |u_{\mathbf{k}}|^2 = \frac{1}{2}\left(1 - \frac{\xi_{\mathbf{k}}}{E_{\mathbf{k}}}\right) \tag{2.17}$$

where

$$E_{\mathbf{k}} = (\xi^2_{\mathbf{k}} + |\Delta_{\mathbf{k}}|^2)^{1/2} \tag{2.18}$$

$E_{\mathbf{k}}$ is the energy of the quasi-particle excitations. Equation 2.18 shows that Δ is indeed an energy gap. Even if $\xi_{\mathbf{k}} = 0$ (at the Fermi surface) a minimum energy Δ is needed for an excitation. $\Delta_{\mathbf{k}}$ in terms of excitations is now given by

$$\Delta_{\mathbf{k}} = -\sum_{\mathbf{l}} V_{\mathbf{kl}} \langle c_{-\mathbf{l}\downarrow} c_{\mathbf{l}\uparrow} \rangle = -\sum_{\mathbf{l}} V_{\mathbf{kl}} u_{\mathbf{l}}^{\dagger} v_{\mathbf{l}} \langle 1 - \gamma_{\mathbf{l}0}^{\dagger} \gamma_{\mathbf{l}0} - \gamma_{\mathbf{l}1}^{\dagger} \gamma_{\mathbf{l}1} \rangle \tag{2.19}$$

2.1.3 Finite temperatures

At finite temperatures the distribution of excitations is given by the usual Fermi function:

$$f(E_{\mathbf{k}}) = (e^{\beta E_{\mathbf{k}}} + 1)^{-1} \tag{2.20}$$

where $\beta = 1/k_B T$. Substituting this for the excitations in equation 2.19 becomes

$$\langle 1 - \gamma_{\mathbf{l}0}^{\dagger} \gamma_{\mathbf{l}0} - \gamma_{\mathbf{l}1}^{\dagger} \gamma_{\mathbf{l}1} \rangle = 1 - 2f(E_{\mathbf{l}}) \tag{2.21}$$

and so Δ becomes

$$\Delta_{\mathbf{k}} = -\sum_{\mathbf{l}} V_{\mathbf{kl}} \frac{\Delta_{\mathbf{l}}}{2E_{\mathbf{l}}} \tanh\left(\frac{\beta E_{\mathbf{l}}}{2}\right) \tag{2.22}$$

The self-consistency condition becomes (with the BCS approximation $V_{\mathbf{kl}} = -V$)

$$\frac{1}{V} = \frac{1}{2} \sum_{\mathbf{k}} \frac{\tanh(\beta E_{\mathbf{k}}/2)}{E_{\mathbf{k}}} \tag{2.23}$$

This equation can also be solved to give an equation for T_c:

$$k_B T_c = 1.13 \hbar \omega_D e^{-1/N(0)V} \tag{2.24}$$

where ω_D is the Debye frequency. Δ depends on temperature, it is zero exactly at T_c and it approaches the value $1.76 k_B T_c$ at T=0. In fig.2.1 a plot of Δ is given.

2.1.4 Bogoliubov-de Gennes equations

In the previous sections the superconductor was homogeneous. Difficulties arise when the superconducting order parameter varies in space, for example at an interface with another material. In these cases we can use the Bogoliubov-de Gennes equations.
Because of the spatial variations of the Hamiltonian, the plane wave momentum eigenfunctions characterized by k which were used in the previous sections can not be used. They must be replaced by position-dependent functions, which can be found using a generalization of the Bogoliubov transformations:

$$\Psi(\mathbf{r} \uparrow) = \sum_{n} [\gamma_{n\uparrow} u_n(\mathbf{r}) - \gamma_{n\downarrow}^{\dagger} v_n^{\dagger}(\mathbf{r})] \tag{2.25}$$

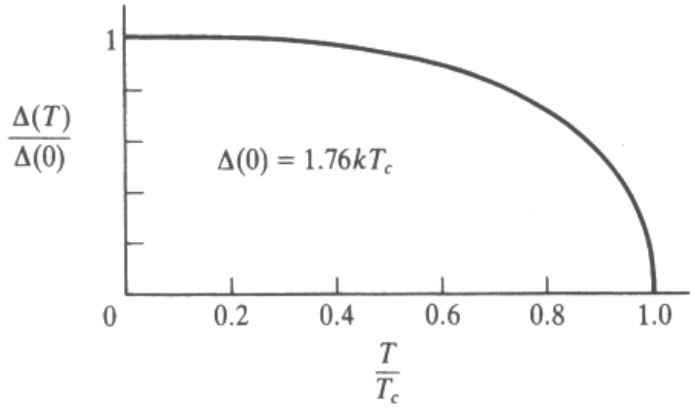

Figure 2.1: *Temperature dependence of the energy gap in BCS theory. It holds for all materials, provided they are in the weak-coupling limit (Figure taken from ref. [6]).*

$$\Psi(\mathbf{r}\downarrow) = \sum_n [\gamma_{n\downarrow} u_n(\mathbf{r}) - \gamma^\dagger_{n\uparrow} v^\dagger_n(\mathbf{r})] \tag{2.26}$$

where the Ψ's are annihilation operators for position eigenfunctions instead of momentum eigenfunctions, as the c's were in the Bogoliubov transformation. The u's and v's are position-dependent eigenfunctions and can be determined by diagonalizing the Hamiltonian:

$$H = \int \Big(\sum_\sigma \Psi^\dagger(\mathbf{r},\sigma) \left(\frac{1}{2m} \left(\frac{\hbar}{i}\nabla - e\mathbf{A} \right)^2 + U(r) - \mu \right) \Psi(\mathbf{r},\sigma) \\ + \Delta(\mathbf{r}\Psi^\dagger((r)\uparrow)\Psi^\dagger((r)\downarrow) + \Delta^\dagger(\mathbf{r}\Psi((r)\uparrow)\Psi((r)\downarrow)\Big) d\mathbf{r} \tag{2.27}$$

where $\Delta(\mathbf{r}) = V\langle\Psi(\mathbf{r}\uparrow)\Psi(\mathbf{r}\downarrow)\rangle = V\sum_n v^\dagger_n(\mathbf{r})u_n((r))(1-f_n)$. $U(\mathbf{r})$ includes electron-electron interactions, electron-ion interactions and any other electrostatic potential. μ is the chemical potential and f_n is the Fermi function. The diagonalization of this Hamiltonian requires that u and v satisfy the following equations:

$$H_0 u(\mathbf{r}) + \Delta(\mathbf{r})v(\mathbf{r}) = Eu(\mathbf{r}) \tag{2.28}$$

$$-H_0^\dagger v(\mathbf{r}) + \Delta^\dagger(\mathbf{r})u(\mathbf{r}) = Ev(\mathbf{r}) \tag{2.29}$$

with

$$H_0 = \frac{1}{2m}\left(\frac{\hbar}{i}\nabla - e\mathbf{A}\right) + U(\mathbf{r}) - \mu \tag{2.30}$$

These equations are the Bogoliubov-de Gennes equations.

2.2 Ginzburg-Landau theory

BCS-theory is excellent when dealing with energy gaps which are constant in space. If not the theory remains valid but becomes very complicated and the more simple Ginzburg-Landau (GL) theory is more useful. GL-theory was proposed in 1950, 7 years before BCS-theory. Using the fact that the superconducting phase transition is a second-order phase transition, Ginzburg and Landau introduced a pseudowavefunction ψ as an order parameter in Landau's theory of second order phase transitions. ψ is in general complex:

$$\psi = |\psi| e^{i\varphi} \tag{2.31}$$

ψ is related to the density of superconducting electrons n_s:

$$n_s = |\psi(x)|^2 \tag{2.32}$$

2.2.1 Free energy

GL postulated that the free energy density near T_c can be expanded as:

$$f = f_{n0} + \alpha|\psi|^2 + \frac{\beta}{2}|\psi|^4 + \frac{1}{4m}\left|\left(\frac{\hbar}{i}\nabla - 2e\vec{A}\right)\psi\right|^2 + \frac{B^2}{2\mu_0} \tag{2.33}$$

with f_{n0} the free energy density in the normal state and in zero field, α and β parameters, m the mass of one electron and e its charge, $\vec{A}$ the vector potential and B the magnetic induction. The superconductor tends as usual to minimize its total free energy. The total free energy can be obtained by integrating over the volume: $F = \int f d^3\vec{r}$. The fact that the free energy has to be minimal requires that $\partial F = 0$. This variational problem can be solved by (standard but cumbersome) methods and leads to the GL differential equations:

$$\alpha\psi + \beta|\psi|^2\psi + \frac{1}{4m}\left(\frac{\hbar}{i}\nabla - 2e\vec{A}\right)^2\psi = 0 \tag{2.34}$$

and

$$\vec{J} = \frac{1}{\mu_0}\nabla \times \vec{B} = \frac{e\hbar}{2mi}(\psi^\dagger\nabla\psi - \psi\nabla\psi^\dagger) - \frac{2e^2}{m}\psi^\dagger\psi\vec{A} \tag{2.35}$$

or

$$\vec{J} = \frac{e}{m}|\psi|^2(\hbar\nabla\varphi - 2e\vec{A}) = 2e|\psi|^2\vec{v}_s \tag{2.36}$$

with $\vec{v}_s$ the supercurrent velocity and $\vec{J}$ is the supercurrent density. These differential equations have to be completed by boundary conditions. A possible choice is

$$\left(\frac{\hbar}{i}\nabla - 2e\vec{A}\right)\psi\Big|_n = 0 \tag{2.37}$$

This assures that no current is passing through the surface and is appropriate at an insulating surface. For a metal-superconductor interface this has to be generalized to:

$$\left(\frac{\hbar}{i}\nabla - 2e\vec{A}\right)\psi\Big|_n = \frac{i\hbar}{b}\psi \tag{2.38}$$

with b a real constant. b is proportional to $\frac{1}{\nabla\psi}$ at the interface. The value of b depends on the material to which contact is made, it can be very large for normal metals and approaches zero for a ferromagnet, with normal metals in between. In fig.2.2 a schematic plot of ψ at an interface can be seen.

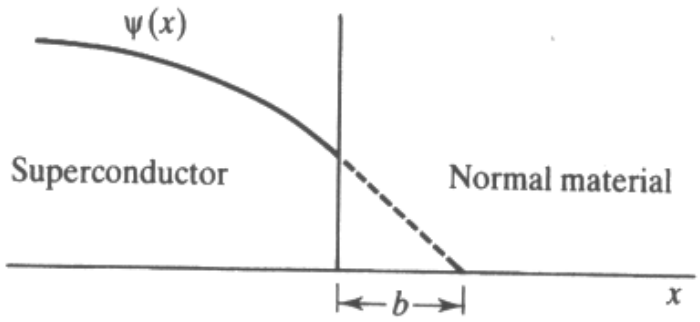

Figure 2.2: *ψ in the neighborhood of a S/N interface. b is the length to the point at which ψ would go to zero if it maintained the slope it had at the surface (Figure taken from ref. [6]).*

In GL theory two characteristic length scales occur. The first one is the penetration depth. The external magnetic field decays exponentially with this length scale, denoted λ_{eff}.

$$\lambda_{eff} = \frac{1}{\sqrt{2}}\frac{1}{1-t}\lambda_L \tag{2.39}$$

where $t = T/T_c$ and λ_L is the London penetration depth.

The other length scale is $\xi(T)$, the characteristic length for variations of ψ. It is defined by

$$\xi^2(T) = \frac{\hbar^2}{4m|\alpha(T)|} \tag{2.40}$$

It is related to, but not the same as ξ_0, the BCS coherence length. The relation close to T_c is

$$\xi(T) = 0.74\frac{\xi_0}{(1-t)^{1/2}} \tag{2.41}$$

for a pure superconductor and

$$\xi(T) = 0.855 \frac{(\xi_0 l)^{1/2}}{(1-t)^{1/2}} \tag{2.42}$$

for a dirty superconductor (l is the mean free path of the electrons). The exact values for the constants are taken from BCS theory.
Another useful parameter is the dimensionless Ginzburg-Landau parameter κ, defined as

$$\kappa = \frac{\lambda_{eff}(T)}{\xi(T)} \tag{2.43}$$

In the pure and dirty limits it gives the following numerical results:

$$\kappa = 0.96 \frac{\lambda_L(0)}{\xi_0} \tag{2.44}$$

for the pure case and

$$\kappa = 0.715 \frac{\lambda_L(0)}{l} \tag{2.45}$$

for the dirty case, again with the numerical values from BCS theory. κ can be used to distinguish type I and type II superconductors. If $\kappa < 1/\sqrt{2}$ it is a *type I superconductor* and if $\kappa > 1/\sqrt{2}$ it is a *type II superconductor*. A type II superconductor is characterized by two critical fields H_{c1} and H_{c2}. If the field is below H_{c1} or above H_{c2} a type II superconductor is not different from a type I superconductor. Between the two fields flux is able to penetrate the superconductor, reaching $B = \mu_0 H$ at H_{c2}. The flux penetrates as an array of flux tubes, called *vortices*, each carrying one flux quantum $\Phi_0 = \frac{h}{2e}$.
If one applies a current to a superconducting material with vortices, the vortices experience a Lorentz force and this gives rise to a resistance. In practice the vortices are usually somehow pinned and they do not move until a certain critical current is reached. At this current suddenly a resistance appears.

2.3 More modern approach

Modern theories use Green function to describe superconductivity. Green functions are defined as solution to certain differential equations but can also be used to describe the theory of superconductivity. The Green function of a normal particle is defined as

$$G_{\alpha\beta} = -i\Big\langle T_t\Big(\psi_\alpha(x)\psi^\dagger_\beta(x')\Big)\Big\rangle_{st} \tag{2.46}$$

where α and β are spin indices, $\psi^\dagger_\alpha(x)$ and $\psi_\alpha(x')$ are electron creation and annihilation operators respectively. x and x' are coordinates (including time)

and T_t is an operator which orders the operators logically in time. $\langle ... \rangle_{st}$ denotes a statistical average over all possible paths from x' to x. Thus this Green function (creating a particle at x' and annihilating it at x) describes the movement of a particle from x' to x. It gives a probability amplitude for a particle, being at time t' and position $\vec{r}'$, to be found at time t at location $\vec{r}$. The Green function has to be complemented by $\overline{G}$, the Green function which describes the opposite movement. $G^* = -\overline{G}$ where * denotes complex conjugate. The Cooper pairs are described by a second type of Green functions, the anomalous Green functions F and $\overline{F}$. They are defined by

$$F_{\alpha\beta} = -i\Big\langle T_t\Big(\psi_\alpha(x)\psi_\beta(x')\Big)\Big\rangle_{st} \tag{2.47}$$

and $F^* = -\overline{F}$. $\overline{F}$ creates two particles at x and x' (Cooper pair) and F annihilates two particles at x and x'.
It is also possible to write Δ in terms of Green functions:

$$\Delta_{\alpha\beta}(x) = -\lambda F_{\alpha\beta}(x,x) \tag{2.48}$$

$$\overline{\Delta}_{\alpha\beta}(x) = -\lambda \overline{F}_{\alpha\beta}(x,x) \tag{2.49}$$

λ is the attractive interaction. If α and β are equal, Δ has to be zero, because in the singlet superconductor described here only unequal spins are correlated and equal spins are not. The anomalous Green function F only describes correlated particles.
For a system described by the BCS Hamiltonian the equations of motion for the time-dependent electron operators are

$$i\hbar\partial_t\psi_\alpha(x) = H_\alpha(x)\psi_\alpha(x) + \lambda\sum(\psi^\dagger_\gamma(x)\psi_\gamma(x))\psi_\alpha(x) \tag{2.50}$$

$$-i\hbar\partial_t\psi^\dagger_\alpha(x) = H^\dagger_\alpha(x)\psi^\dagger_\alpha(x) + \lambda\psi^\dagger_\alpha(x)\sum(\psi^\dagger_\gamma(x)\psi_\gamma(x)) \tag{2.51}$$

where $H^{(\dagger)}_\alpha(x)$ is the BCS Hamiltonian:

$$\begin{aligned} H_{BCS} = &-\sum\Big(\psi^\dagger_\alpha(\vec{r})\frac{\hbar^2\nabla^2}{2m}\psi_\alpha(\vec{r})\Big) + \\ &\frac{\lambda}{2}\sum\Big(\psi^\dagger_\beta(\vec{r})\psi^\dagger_\alpha(\vec{r})\psi_\alpha(\vec{r})\psi_\beta(\vec{r})\Big) \end{aligned} \tag{2.52}$$

This equation can now be rewritten to become an equation for the Green functions of the system. This leads to equations of the form

$$[\hbar\partial_\tau + H(x)]G_{\alpha\beta}(x,x') - \sum_\gamma \Delta_{\alpha\gamma}(x)\overline{F}_{\gamma\beta}(x,x') = \hbar\delta(x-x')\delta_{\alpha\beta} \tag{2.53}$$

τ is the imaginary time, $\tau = it$. Combining all things together results in the Gor'kov equation (better: equations). These equations for all possible combinations of spin directions can be combined in a single matrix (to save space):

$$[\hbar\partial_\tau(\sigma_0 \otimes \tau_3) + H_0(x)(\sigma_0 \otimes \tau_0) - \check{\Delta}(x)]\check{G}(x,x') = \hbar\delta(x-x')(\sigma_0 \otimes \tau_0) \tag{2.54}$$

The free space we saved can now be used to explain the notation. H_0 is still the BCS Hamiltonian. $\check{G}(x,x')$ is the Gor'kov matrix.

$$\check{G}(x,x') = \begin{pmatrix} \hat{G}(x,x') & \hat{F}(x,x') \\ \hat{\overline{F}}(x,x') & \hat{\overline{G}}(x,x') \end{pmatrix}$$

and $\hat{G}(x,x')$ is defined as

$$\hat{G}(x,x') = \begin{pmatrix} G_{\uparrow\uparrow}(x,x') & G_{\uparrow\downarrow}(x,x') \\ G_{\downarrow\uparrow}(x,x') & G_{\downarrow\downarrow}(x,x') \end{pmatrix}$$

and similar for the other Green functions. $\check{\Delta}(x) = \begin{pmatrix} 0 & \hat{\Delta}(x) \\ \hat{\overline{\Delta}}(x) & 0 \end{pmatrix}$ with $\hat{\Delta} = \begin{pmatrix} 0 & \Delta_{\uparrow\downarrow}(x) \\ \Delta_{\downarrow\uparrow}(x) & 0 \end{pmatrix}$ and $\hat{\overline{\Delta}} = \begin{pmatrix} 0 & \overline{\Delta}_{\uparrow\downarrow}(x) \\ \overline{\Delta}_{\downarrow\uparrow}(x) & 0 \end{pmatrix}$ The σ-terms are the Pauli spin matrices: $\sigma_0 = \begin{pmatrix} 1 & 0 \\ 0 & 1 \end{pmatrix}$, $\sigma_1 = \begin{pmatrix} 0 & 1 \\ 1 & 0 \end{pmatrix}$, $\sigma_2 = \begin{pmatrix} 0 & -i \\ i & 0 \end{pmatrix}$, $\sigma_3 = \begin{pmatrix} 1 & 0 \\ 0 & -1 \end{pmatrix}$ The τ-terms are the same matrices, the only difference is that a σ-matrix describes simple electron spins and a τ-matrix describes a particle-hole built quasiparticle.

The Gor'kov equations contain the same information as the original BCS equations (no approximations are made) and are not easier to solve. In practice certain approximations have to be made and they can be made because there is a lot of information in the equations that we do not use. The characteristic length scale of a superconductor, ξ_0, is much larger than the Fermi wavelength and because of that we can throw away (average out) all features that have a characteristic wavelength in the order of the Fermi wavelength. So we can simplify the equations by averaging these oscillations out. This procedure is known as the quasi-classical approximation. It includes a change in variables (the two separate coordinates of the two particles are changed into a center-of-mass coordinate and a relative coordinate) and an integration over the relative coordinate. This results in

$$-i\hbar\vec{v_F}\partial_R\check{g} + (\sigma_0 \otimes \tau_3)\hbar\partial_\tau\check{g} + \hbar\partial_{\tau'}\check{g}(\sigma_0 \otimes \tau_3) - \check{\Delta}(\vec{R},\tau)\check{g} + \check{g}\check{\Delta}(\vec{R},\tau') = 0 \tag{2.55}$$

where $\vec{v_F}$ is the Fermi velocity, $\check{\Delta}(\vec{R},\tau) = \begin{pmatrix} 0 & \hat{\Delta}(\vec{R},\tau) \\ \hat{\overline{\Delta}}(\vec{R},\tau) & 0 \end{pmatrix}$ and $\check{g}(\vec{R},\hat{\vec{p}},\tau,\tau') = \begin{pmatrix} \hat{g}(\vec{R},\hat{\vec{p}},\tau,\tau') & \hat{F}(\vec{R},\hat{\vec{p}},\tau,\tau') \\ \hat{\overline{F}}(\vec{R},\hat{\vec{p}},\tau,\tau') & \hat{\overline{g}}(\vec{R},\hat{\vec{p}},\tau,\tau') \end{pmatrix}$. The Green functions are now quasi-classical, which means that they depend on the center-of-mass coordinate $\vec{R}$ and the direction of the momentum ($\hat{\vec{p}}$ is a unit vector in the direction of the momentum) instead of two separate sets of coordinates for each particle. In general the assumption is that the $\uparrow$ and $\downarrow$ electrons are in identical spin bands and thus have identical Fermi velocity. This assumption is wrong in case of a S/F bilayer where S is the superconductor and F a strong ferromagnet, because a strong ferromagnet is not supposed to have equal spin bands. However, the assumption is fulfilled in case of a weak ferromagnet.

If the superconductor is a dirty-limit material a further approximation can be made. In such material the impurity density is high and the electrons have a very short mean free path. They scatter very often before dephasing and after a few collisions they do not remember the initial direction they were going. The material then becomes isotropic. The superconductor can now be described by the Usadel equation:

$$i\hbar D\nabla(\check{g}\nabla\check{g}) = -i\hbar[H,\check{g}] \tag{2.56}$$

D is the diffusion constant, depending on the Fermi velocity and the electron mean free path, $D = \frac{1}{3}v_F l_e$. H is a matrix which has the electron energy eigen values on the diagonal and the off-diagonal elements are the terms which represent the gap.

Chapter 3

Ferromagnetism

A ferromagnet is a material in which all magnetic moments at the atoms are aligned in the same direction[1] [7]. It has a spontaneous magnetization even in absence of a magnetic field. At low temperatures, below T_{Curie}, the ferromagnetic transition temperature, the material has a ferromagnetic ground state. Above T_{Curie} the ferromagnetism is destroyed and the material shows only paramagnetic behavior, which means that an external magnetic field will align the magnetic moments in the same direction as the field. In nature the only elements that could possibly show ferromagnetic behavior are 3d elements (Sc, Ti, V, etc.) and 4f elements (rare earth metals like Gd). The discussion will be confined to so called band ferromagnets which Py (permalloy, $Ni_{80}Fe_{20}$) is, consisting of two 3d elements.
In such an alloy the ferromagnetism can be described in terms of an exchange interaction between the electrons. The electrons are divided into two subbands, one for each spin. The number of spin up electrons $n_\uparrow$ and the number of spin down electrons $n_\downarrow$ is not equal. The kinetic energies of electrons at the Fermi energy of the two subbands are given by ($n_\uparrow > n_\downarrow$)

$$E_{F\uparrow}^{kin} = E_{F,N} + \delta E \tag{3.1}$$

$$E_{F\downarrow}^{kin} = E_{F,N} - \delta E' \tag{3.2}$$

$E_{F,N}$ is the energy without exchange interaction. δE and $\delta E'$ are the energy differences due to the exchange interaction. They are not necessarily equal. The total kinetic energy of the electrons is now higher than when the subbands are equally occupied. But this is balanced by the exchange interaction which lowers the total energy. For ferromagnetism to occur the following criterion has to be fulfilled:

$$Ug(E_F) \geq 1 \tag{3.3}$$

the so called *Stoner criterion*. U is a measure for the strength of the exchange interaction and $g(E_F)$ is the density of states at the Fermi energy. It says that

[1] ignoring the presence of domains and domain walls

for ferromagnetism to occur it is necessary that the exchange interaction is high enough and the density of states at the Fermi energy is high enough. Of all 3d elements this is only satisfied in Fe, Co and Ni.

3.1 Domains and domain walls

In an ideal ferromagnetic sample all magnetic moments are aligned in one direction. In a real sample however *domains* can occur: In the material small regions can be distinguished, the domains. Within each region the spins are pointing in the same direction. Instead of global alignment now we have regions which all have their own alignment, separated by *domain walls*. In the domain walls the direction of the magnetization changes to that of the adjacent domain. Sizes of domain walls are small compared to the size of domains.
There are various types of domain walls. A 180 ° domain wall separates domains of opposite magnetization, a 90 ° domain wall separates domains with perpendicular magnetization. A common type of 180 ° wall is a *Bloch wall*. In a Bloch wall the magnetization is rotating in a plane parallel to the plane of the wall (see fig.3.1). Another type of wall is the *Néel wall*. In a Néel wall the magnetization rotates in a plane perpendicular to the plane of the wall.

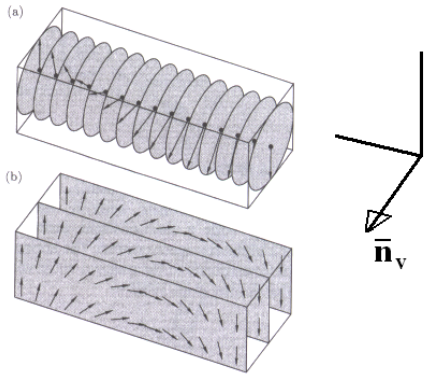

Figure 3.1: ***a*** *Bloch wall and* ***b*** *Néel wall. The vector normal to the thin film plane is indicated as* $\bar{\mathbf{n}}_\mathbf{v}$ *(Figure taken from ref. [7]).*

One can wonder why a ferromagnetic material wants to make domains, since the exchange energy tends to align all spins in the same direction and therefore a domain wall and the presence of differently oriented domains costs energy. The reason is that there is another energy involved, the dipolar energy. The dipolar energy wants to lower the total magnetization of the whole sample. If at the edges the magnetization is pointing out of the sample it costs energy because the space surrounding the sample is filled with demagnetizing fields. This energy can

be saved by breaking the sample into domains, which costs energy with respect to the exchange energy but saves energy due to demagnetizing fields.
Due to the crystal structure a sample can have easy and hard axes. The easy axis is the axis along which the sample is easy to magnetize, only a small field is needed. The hard axis is the opposite, a high field is needed to magnetize the sample in this direction. In a very small sample also $E_{anisotropic}$ can be important. It tends to align the direction of magnetization with the long axis of the sample as it is energetically very unfavorable to align it perpendicular to the long axis, it costs dipolar energy. This causes that in a long and narrow strip a stable domain configuration is not easy to establish, except for some domains at the end of the strip.
Dipolar energy can also determine the type of domain that can be formed. In a bulk sample a Bloch wall is favored. In a thin sample a Néel wall tends to be favored. In such a sample it is energetically very unfavorable to rotate spins out of the plane of the film.

3.2 Hysteresis

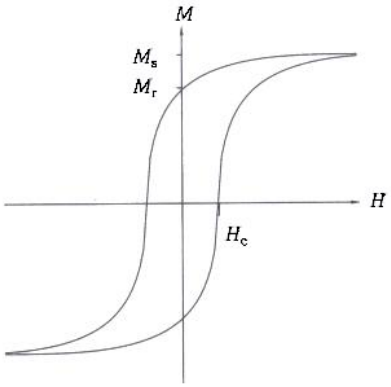

Figure 3.2: *Typical hysteresis loop for a ferromagnet. Indicated are the saturation magnetization M_s, the remanent magnetization M_r and the coercive field H_c (Figure taken from ref. [7]).*

In fig.3.2 a typical curve of magnetization as function of applied magnetic field is shown. It shows a hysteresis loop; if the applied magnetic field is increased high enough the magnetization will reach the *saturation magnetization* M_S. The magnetization of the whole sample is pointing in the direction of the external field. If the field is reduced the magnetization starts to rotate toward its easy directions, domains walls are not yet moving. In general this happens without hysteresis, the loop does not open yet. If the field is decreased further domains walls start to

move. The walls jump from one local minimum to another and this process is not reversible, it shows hysteresis. Following the hysteresis loop the field is reduced to zero and the magnetization reduces to the *remanent magnetization* M_r. If then the field again increases but now in opposite direction the magnetization finally becomes zero at the *coercive field* H_c. Finally the domain walls stop moving and the hysteresis closes. The last part towards the saturation magnetization the magnetization in the domains rotates to the direction of the external field. It is now entirely magnetized in opposite direction. In the same way the direction of magnetization changes back to the original direction .

3.3 Anisotropic magnetoresistance

The change in resistance of a sample when placed in an external magnetic field is called *magnetoresistance* [8]. The straightforward mechanism is of course the Lorentz force experienced by a moving electron. The electron is now deflected and begins to orbit until it is scattered. Because the curved orbit is longer than the straight one and the concentration of scatterers is the same, the electron is scattered more often, causing higher resistance. According to this simple picture the resistance in a magnetic field is always higher than without field. This is called ordinary magnetoresistance (MR). However, a much more important mechanism in ferromagnets is the *anisotropic magnetoresistance (AMR)*. In a material showing AMR behavior the resistance does not depend only on the applied field but also (more important) on the actual direction of the magnetization with respect to the current flow (that is why it is called anisotropic). In most cases (also in Py) the resistance is highest if current and magnetization are parallel and lowest if they are perpendicular to each other. Because AMR depends on magnetization, it shows hysteresis. In this way it is possible that the resistance in field is lower than the resistance in zero field.

3.3.1 Origin of AMR effect

AMR can not be explained by the mechanism of the ordinary MR effect. A (not entirely satisfactory) explanation needs the following ingredients: two-current model, spin-orbit interaction and s-d scattering depending on the direction of magnetization (all to be explained below). The explanation is given for strong d-band ferromagnetic Ni-based alloys.

Two current model. Below T_{Curie} the total amount of spin up electrons and spin down electrons is conserved and therefore also the current carried by spin up and spin down electrons. So it makes sense to consider the spin up and spin down electrons as being two separate channels along which conduction can take place. Each channel has its own diffusion constant at the Fermi level D_F,

Fermi velocity v_F and density of states at the Fermi level N_F. The current is carried by electrons near or at the Fermi level and the resistance of the channel is determined by these electrons. The resistivity of the spin up channel is denoted as $\rho_\uparrow$ and the resistivity of the spin down channel as $\rho_\downarrow$. In general $\rho_\uparrow$ and $\rho_\downarrow$ are not equal. This is the case since D_F, v_F and N_F are all unequal for the two channels. The d band of the majority spin channel (denoted as $d_\uparrow$) is full and the other one ($d_\downarrow$) is not. As a result $s_\uparrow$ electrons can not be scattered in the $d_\uparrow$ band. s electrons are mainly responsible for the transport, d electrons are more localized and have therefore a higher resistance. The absence of s-d scattering for the majority channel leads to a lower resistance. In the other channel s-d scattering is possible and there the resistance is higher.

Spin-orbit interaction. Spin-orbit interaction (SOI), the coupling between the electron orbital motion and its spin, provides a way to mix the $\uparrow$ and $\downarrow$ channels. The SOI operator is given by

$$\mathbf{L} \cdot \mathbf{S} = L_x S_x + L_y S_y + L_z S_z = L_z S_z + \frac{1}{2}(L^+ S^- + L^- S^+) \tag{3.4}$$

where $L^\pm = L_x \pm iL_y$ and $S^\pm = S_x \pm iS_y$ and $\mathbf{S}$ and $\mathbf{L}$ are the spin and orbital angular momenta respectively. The effect of $L^\pm$ is raising or lowering the m_l value of the electron. $S^\pm$ raises or lowers the spin quantum number. The operator in equation 3.4 therefore acts as spin-flip operator and is able to mix the $\uparrow$ and $\downarrow$ channels. It takes $3d_\uparrow(m_l)$ states into $3d_\downarrow(m_l{+}1)$ states or $3d_\downarrow(m_l)$ states into $3d_\uparrow(m_l{-}1)$ states. Now there are $3d_\uparrow$ holes and $s_\uparrow$ electrons can be scattered in these holes, and the resistance of the $\uparrow$ band is now higher than without SOI.

Resistance anisotropy. With SOI $s_\uparrow$ electrons can scatter to $3d_\downarrow$ states. It also allows $d_\uparrow \rightarrow s_\downarrow$ transitions. This opens more $3d_\uparrow$ hole states and allows more s-d scattering by $s_\uparrow$ or $s_\downarrow$ electrons. But s electrons can only scatter into 3d hole states if their momentum is in the plane of the classical orbit of the empty d state. The magnetization causes states with orbits perpendicular to the direction of magnetization to be filled first, leaving those with orbits along the magnetization direction empty. s electrons can only scatter in these d holes if the magnetization is parallel to the current direction.

Conclusion According to the two-current model there are two separate channels, one for $\uparrow$ electrons and one for $\downarrow$ electrons. Taking $\uparrow$ as the majority spin band, the resistance in the $\uparrow$ channel is lower than in the $\downarrow$ channel because the $d_\uparrow$ band is full and electrons can not scatter to this band. SOI provides a method to mix the spin channel. Now there are empty $d_\uparrow$ states and it is possible to scatter to the $d_\uparrow$ band. But it depends on the direction of the magnetization if there are empty states available. If the magnetization is parallel to the current

direction s-d scattering is possible and then the resistance becomes higher. In total it means that the resistance of a Py sample is lower if the magnetization is perpendicular to the direction of the current than if the magnetization is parallel to the direction of the current.

Chapter 4

Proximity effect

4.1 S/N structures

When a superconductor is in contact with a normal metal, Cooper pairs can enter the normal metal by undergoing an *Andreev reflection*, and vice versa, an electron in the normal metal can enter the superconductor at energies inside the band gap by the same mechanism. In fig.4.1 the mechanism of the Andreev reflection is explained. An electron e_1 wants to enter the superconductor but it is not allowed because it has an energy inside the gap, there are no eigenstates having the same energy as e_1. However, instead of a reflection at the interface it can undergo an Andreev reflection. The electron takes an extra electron e_2 from its environment and enters the superconductor as a Cooper pair. In the normal metal a hole is moving back along the path of the original electron. The spin and momentum of the hole are opposite to those of the electron. If an electron from a Cooper pair wants to enter the normal metal the procedure takes place in reversed order.
Close to the interface the normal metal will get some superconducting properties, while the Cooper pair density in the superconducting material will decrease which results in a locally suppressed gap near the interface. The region over which the normal metal gains some superconducting properties is determined by the spatial existence of Cooper pairs inside N. The Cooper pair density in the normal metal will decay exponentially in space. The characteristic length scale of this decay is called the normal metal coherence length, $\xi_N \sim \sqrt{\frac{\hbar D}{k_B T}}$. Here it is assumed that temperature is the main force which can break pairs and that we are in the diffusive limit. This is always the case when using thin films. D is the *diffusion constant*. When it is large, it means that a electron can travel a long distance without *dephasing*. Inside S the formation of a Cooper pair takes place over a certain length. This distance is the S coherence length, ξ_S.

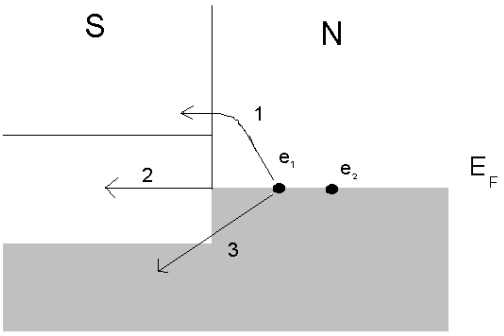

Figure 4.1: *mechanism of Andreev reflection. The electron e_1 with momentum k wants to enter the superconductor from the normal metal. It can not follow path 1, because it does not have enough energy. Path 2 is not possible because there is a gap and inside the gap are no states available. Path 3 is not possible either because there all states are already filled. The only possibility is to take another electron e_2 with it and enter the S material together as Cooper pair. e_2 leaves a hole which travels backwards with momentum -k*

4.1.1 BTK theory

In 1982 G.E.Blonder, M. Tinkham and T.M. Klapwijk (BTK) described the possible mechanisms taking place at an S/N interface [9]. They started from the Bogoliubov-de Gennes equations (equations 2.28 and 2.29) and recognized that in the superconducting state for each eigenvalue four different values for k exist (k^+, k^-, $-k^+$ and $-k^-$, k^+ is outside the Fermi sphere, k^- is inside the Fermi sphere), which all have E_k. Transitions from one k state to another are all energetically allowed, but there is another constraint, namely that a particle which travels with positive group velocity can only produce transmitted particles with positive group velocity and reflected ones with negative group velocity. According to BTK an electron with energy E_k, momentum k^+ and spin up approaching a N/S interface from the N side has four possibilities (see fig.4.2 and fig.4.3 for the probabilities):

- Andreev reflection. ($\Delta > E_k > 0$) A Cooper pair enters the superconductor and a hole with E_k, k^- and spin down is back reflected.
- ordinary reflection. ($E_k > 0$) An electron is reflected back into the normal metal. This is only possible if the interface is not fully t+ransparent. Fully transparent interfaces mainly exist in theoretical systems.

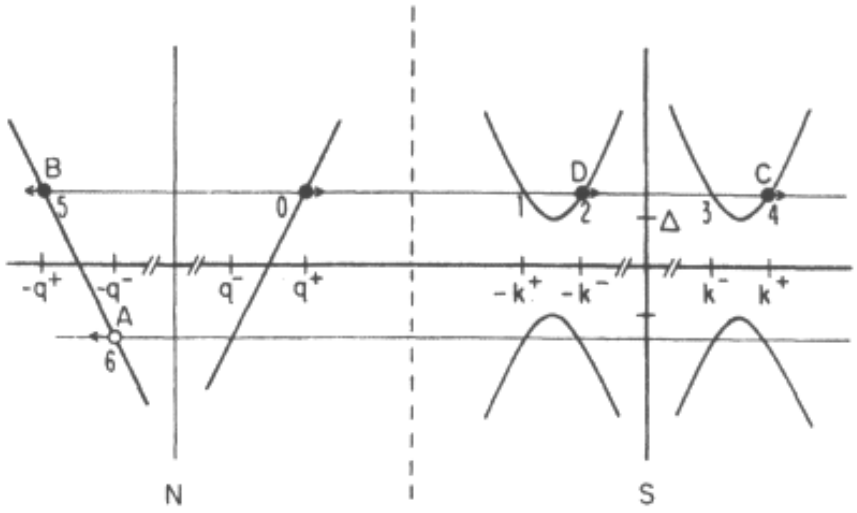

Figure 4.2: *Schematic diagram of energy vs. momentum at a S/N interface. 0 is the incident electron. 2,4,5 and 6 are the possible resulting particles. 2 is an electron transmitted with branch crossing, 4 is a ordinary transmitted electron, 5 is a ordinary reflected electron and 6 is a reflected hole resulting from an Andreev reflection (Figure taken from ref. [9]).*

- ordinary transmission. ($E_k > \Delta$) An electron enters the superconductor as quasi-particle. This is only possible if the electron has an energy higher than the gap.
- transmission with branch crossing. ($E_k > \Delta$) The electron now has momentum $-k^-$ instead of k^+.

4.2 S/F structures

If the neighboring material is a ferromagnet, the Cooper pair density not only decays exponentially but also oscillates in space [10]. The characteristic length scale of the exponential decay, the ferromagnetic coherence length ξ_F, is usually much smaller than ξ_N. Instead of T, we now have $E_{ex} \gg k_B T$ that does the dephasing: $\xi_F \sim \sqrt{\frac{\hbar D}{E_{ex}}}$. If a Cooper pair enters the ferromagnet the spin of only one electron is parallel to the exchange field. The other one is antiparallel. The electron with parallel spin looses potential energy and to conserve the total energy its kinetic energy and therefore momentum will be higher. The potential energy of the other electron will be higher and the kinetic energy and momentum lower. As a result the Cooper pair has got a momentum $|k_\uparrow - k_\downarrow| > 0$ and this gives an oscillation in space. This is superimposed on the normal exponential

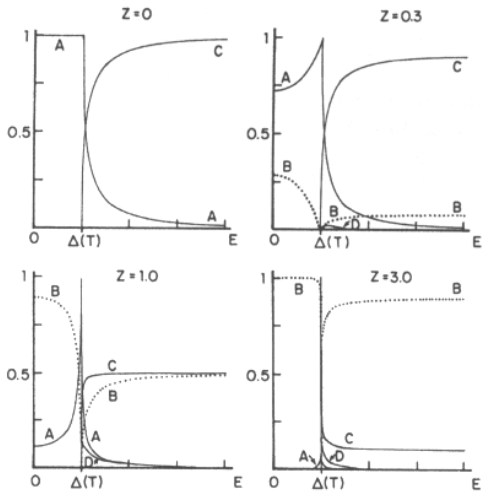

Figure 4.3: *Plots of transmission and reflection coefficients. Z is a measure for the barrier strength at the interface. A gives the probability of an Andreev reflection, B gives the probability of reflection, C gives the probability of transmission without branch crossing and D gives the probability of transmission with branch crossing. Andreev reflections are most probable at energies below the gap, ordinary transmission is only possible if the electron has an energy above the gap. The probability of transmission with branch crossing is always very small (Figure taken from ref. [9]).*

decay. In fig.4.4 the oscillating behavior is shown. The oscillating behavior of the order parameter will cause all quantities related to Δ to oscillate as well. For example the T_c of a S/F bilayer will have an oscillating decay dependence on the F-layer thickness.

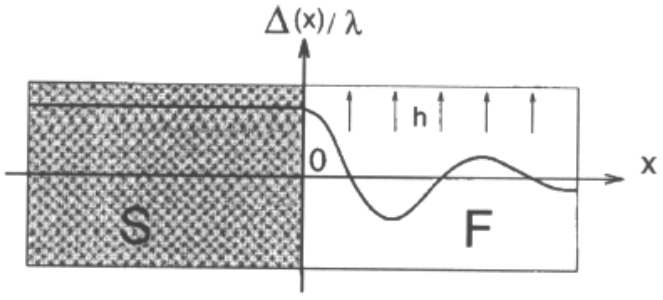

Figure 4.4: *Oscillating behavior of the superconducting order parameter (Figure taken from ref. [10]).*

4.2.1 Andreev reflection at an S/F interface

We can expect that the properties of Andreev reflections at an S/F interface are different from those at an S/N interface [11]. Andreev reflections do not conserve spin, an incoming spin-up electron produces an Andreev-reflected spin-down hole (and a spin-down electron produces a spin-up hole). This is irrelevant if the material is a normal metal but becomes relevant for a ferromagnet because the two subbands are not equally occupied. We assume that the spin-up band is the majority band. Then every incoming spin-down electron can be Andreev-reflected into a spin-up hole. But not every spin-up electron can be Andreev-reflected because there are not enough hole states in the minority band. This means that the Andreev reflections are effectively suppressed.

4.3 F/S/F structures

The behavior of S/F structures leads to the idea that an F/S/F structure can be switched from superconducting state to normal state by the relative orientation of the magnetization of the F layers. This case was predicted theoretically by Tagirov [1] and Buzdin [2] in the limit of a *weak ferromagnet*. A weak ferromagnet means that $E_{ex} \ll E_F$ and that there is no polarization. They examined an F/S/F structure consisting of two identical F layers with a S layer in between. One of the F layers is pinned by an antiferromagnet. In this way it is possible to have a *parallel (P)* or *antiparallel (AP)* configuration of the direction of the exchange fields. They found that a P configuration suppresses the superconductivity more than an AP configuration. If the parameters are chosen properly, it should even be possible to turn the superconductivity on and off by changing the direction of the magnetization in one of the F layers and therefore it acts as a spin switch. The origin of this behavior is that in the AP case the effects of both F layers cancel each other, superconductivity is less suppressed. In the P case the layers do not cancel, but enhance each other and superconductivity is more suppressed. This was confirmed experimentally by Gu et al.[3]. However, Rusanov et al. showed that the strong ferromagnet they have used yield the opposite effect [4]. They used a different method to obtain a parallel and antiparallel configuration, the usage of two different Py thicknesses. The thicker layer is assumed to switch at lower fields than the other one. In this way it is possible to switch between parallel configuration at low fields, antiparallel at higher fields and again parallel at high fields. Apparently S/F structures with weak ferromagnets are quite different from those with strong ferromagnets. A suitable theory of S/F structures with strong ferromagnets is not available. We try to shed more light upon the strong F/S mechanisms.

4.3.1 Prediction for an ideal F/S/F spin switch

We assume that we have an ideal F/S/F spin switch. It is a sample with two Py layers (thickness 50 and 20 nm) which switch independently. They do not influence each other. The structure is small and there is no stable domain configuration. We expect that in such a structure the transmission of Cooper pairs to the normal metal by Andreev reflection is very low. In an AP-state the pair can enter the F-layers, both electrons can enter the majority spin band of one of the layers. In the P-state this is not possible and the pair has to stay in the S-layer. Therefore we expect that $T_c^P > T_c^{AP}$. This is different from a sample with weak ferromagnets. A Cooper pair can enter a weak ferromagnet both in P-state and AP-state. In P-state the electrons of the Cooper pair in the ferromagnet obtain different potential energies and this leads to fast pair breaking and therefore depletion of Cooper pairs at the S-side of the interface and a higher resistance. In AP-state this does not happen, the electrons obtain the same potential energy and the dephasing is less fast.
We will now return to the samples with strong ferromagnets. If we measure R vs. H at a stable temperature in the transition, we expect that the resistance in the P-state is lower than in the AP-state. The resulting curve looks as in fig.4.5. The measurement is performed as follows:

- Saturation at large negative field. The magnetization of both layers is now certainly pointing in the direction of the field.
- Field is decreased to zero. Layers stay in parallel configuration.
- Field is increased in opposite direction. At 5 mT the 50 nm layer switches almost instantaneously. The layers are now antiparallel. The resistance of the sample increases.
- At 10 mT the second layer switches. The layers are now again parallel and the resistance decreases.
- Saturation at large positive field and measurement of the opposite direction. The switching fields are now at -5 mT and -10 mT respectively.

We can also measure R vs. H at a temperature above the transition. We then measure the AMR effect of the Py layers. The expected result is shown in fig.4.6. The resistance decreases if the magnetization in the layers is perpendicular to the direction of the current. This is only the case exactly at the field where one of the layers switches and it produces large spikes.

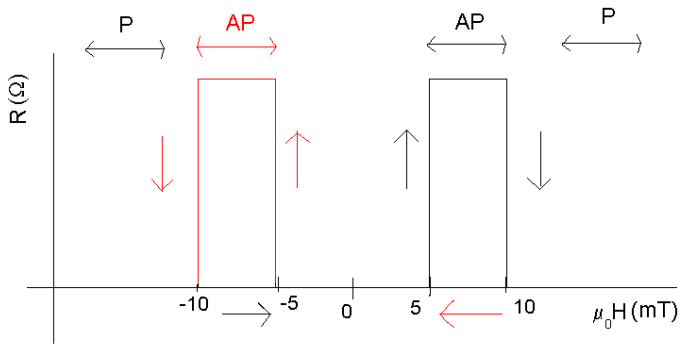

Figure 4.5: *Predicted result of a RH measurement in the transition. The switching fields are at 5 mT and 10 mT. Between 5 and 10 mT the configuration is antiparallel and parallel otherwise. The antiparallel configuration has a higher resistance.*

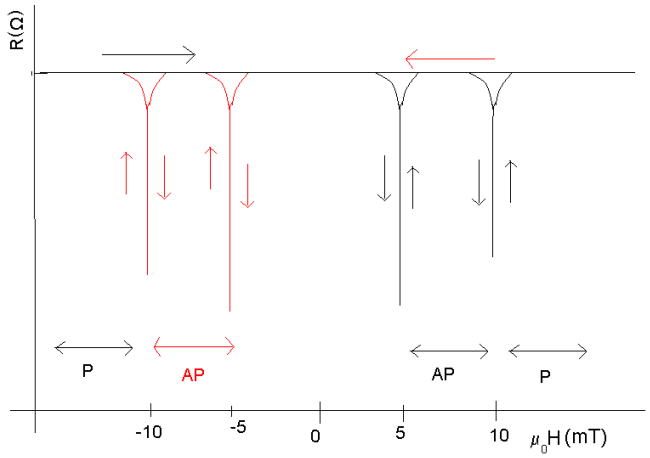

Figure 4.6: *Predicted AMR effect. The sample is the same as in fig.4.5. The resistance is only lowered if one of the layers switches at its switching field.*

Chapter 5

Experimental methods

To investigate the properties of an F/S/F spinvalve we used Py as ferromagnet and Nb as superconductor. Nb is a material with a relatively high T_c (9.3 K for bulk Nb) and it is also easy to sputter. Py ($Ni_{80}Fe_{20}$) is a strong ferromagnet, E_{ex} is approximately 270 meV and it is 45 % spin polarized [5]. The Py/Nb/Py layers were DC sputtered onto clean Si substrates in a UHV system. The base pressure was $\sim 1 \cdot 10^{-9}$ mbar. The used Ar pressure was 4.0 μbar for Nb sputtering and 2.5 μbar for Py sputtering. Some samples have a 2 nm Nb capping layer to prevent oxidation of the top Py layer. This Nb layer does not become superconducting. Magnetic sample holders were used to know with certainty the magnetic field during sputtering because there is also a stray field in the UHV from the targets and the direction of this stray field is not exactly known. The direction of the magnetic field during sputtering determines the easy axes of the Py layers. After sputtering the samples were patterned in strips by e-beam lithography (typically 1 μm$\times$40 μm) and etched using an Ar plasma.
The strips are along the direction of the easy axis. Finally Au contacts were made using a lift off procedure. The Au contacts were sputtered in the ATC. This is a DC sputter system with a base pressure of about $2 \cdot 10^{-7}$ Torr. Ti was used as adhesion layer. The used Ar pressure was 3 mTorr. The contacts consisted of $\sim$5 nm Ti and 100 nm Au.[1] These contacts were used to perform four point measurements. The voltage contacts were 10 μm apart and only this part in the middle was measured. The samples were measured with the magnetic field parallel to the strip. For all samples was performed: RT measurement to determine T_c, for some samples in several fields, RH measurements in the transition and above the transition as well, for some samples the resistance was measured up to a higher field and for some IV curves were made. Samples with T_c's less than 2.5 K (with 20 nm Nb or less) were measured in a ^{3}He cryostat. The others were measured in a PPMS and/or in a standard ^{4}He cryostat. The ^{3}He cryostat is able to measure down to $\pm$300 mK. There is a small magnet which

[1] Further details on sample preparation are given in appendix A. The dimensions and thicknesses of the measured samples can be found in appendix B.

can produce fields from 0 mT to ±50 mT. The resistance was measured using a lockin amplifier. This means that it is an AC measurement, but the results do not differ much from a DC measurement. The used current was 1 or 10 μA. IV curves were made using both a DC and AC signal and so at the same time dV/dI was determined. The other samples were measured using DC current only.
T_c is determined using a 50% criterion; T_c is the temperature where the resistance is decreased to 50% of the value above the transition. The transition width (ΔT_c) was measured between the data points at 10% and 90% of the value of the resistance above the transition. All T_c's were measured in a magnetic field to be sure that the state of the Py layers is the same in all sample (saturated in one direction). Usually a field of 50 mT was applied (20 mT for samples measured in the ^{3}He cryostat).
We also have done some RH measurements in and above the transition because we want to manipulate the direction of the exchange field of the Py layers with the external field. We usually measured the range ±20 mT. A typical measurement would be: saturation at -100 mT to obtain a parallel state and measure from -20 mT to +20 mT. We expect the antiparallel or otherwise non-parallel state to be between 0 and +10 mT. After that we do the reverse measurement.

Chapter 6

Results and discussion

6.1 AMR

6.1.1 Bilayers

We want to compare P and AP states and therefore we need to know the state of the F layers in our trilayer very well and control the switching of the layers. To understand better the behavior of the trilayers we investigate the switching first in bilayers to see how the individual layers behave. Two bilayers were made with 20 nm and 50 nm Py (bi20 and bi50), each with 10 nm Nb. The dimensions of both samples were 40 μm $\times$2 μm. In fact they were made as if a trilayer with 20 nm Nb was cut in the middle of the Nb and divided into two separate samples. The samples did not become superconducting, possibly due to localization effects. This is not surprising, because a trilayer with 20 nm Nb is already very close to the critical thickness of the system. For both samples AMR was measured at 2.0 K. The current and the applied field were both parallel to the long axes of the strip. In fig.6.1 the results are shown for the 20 nm and 50 nm bilayer. The 20 nm bilayer shows a clear, reasonably symmetric AMR effect, with 1.5% resistance change. We see the formation and movement of domains over abroad field range of more than 10 mT, followed by a sharp switch back towards the homogeneous state. The measurement shows that the switching field of the 20 nm layer is around $\pm$10 mT. The 50 nm bilayer sample does not show any AMR effect at all. Not shown is a non-hysteretic dependence of the resistance on the field of 0.08% of the total resistance. Most likely the layer switches very fast and therefore we do not see it. The field steps in the measurement were 0.5 mT. This measurement does actually look like the prediction in fig.4.6. Because the field steps are too large, we can not see the spikes. It is the 20 nm sample which does unexpected things.
The two samples seem to behave very differently. The main differences between the samples are the thickness and the domain wall type. The 50 nm sample has Bloch walls while the 20 nm sample has Néel walls [12]. The thickness causes that

the 50 nm layer carries more current and that an AMR signal (if there is any) will be more visible, assuming that an AMR effect will have the same amplitude in both layers. Because we see no AMR in the thickest layer, this is not simply due to thickness alone. It is possible that Bloch walls can move easier than Néel walls. Then a sample with Bloch walls can produce spikes but a sample with Néel has much larger and broader dips. It is also possible that in the 20 nm sample the Néel walls can cause a more stable domain configuration in the middle of the strip where Bloch walls can occur at the ends of the strip. The length of the strip is 40 μm but we measure only 10 μm in the middle of the strip. Domains nucleated at the ends of the strip are not measured. Since a thicker layer should enhance AMR, most likely it is a change in nucleation points and stable domain configurations; a 20 nm layer has domains in the strip, a 50 nm layer has not.
The following explanations are not believed to be real possibilities: (1) The layer does not switch. This seems impossible because in large negative field the magnetization should be in the opposite direction of the direction in large positive field. (2) The layer switches but there is no current passing through this layer and therefore no AMR. This seems improbable because then all the current should pass through the thin Nb layer instead of the thick Py layer (the resistivities are comparable).
Although we can not measure it directly, the 50 nm layer is believed to switch around 5 mT.

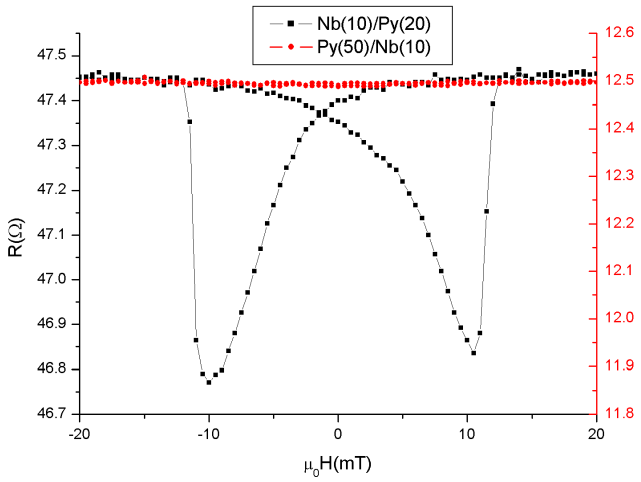

Figure 6.1: *The AMR effect in a bilayer with 10 nm Nb and 20 nm Py and in a bilayer with 50 nm Py and 10 nm Nb. The sample with 20 nm Py shows 1.5% AMR. It switches at 10 mT. The other sample does not show AMR.*

6.1.2 trilayers

Our trilayers show different types of AMR behavior, depending on their dimensions. A trilayer is not just a combination of the two independent bilayers. We have found two types of AMR behavior in different trilayers. None of them looks similar to the prediction (fig.4.6) or to the measurements of the bilayers. The first type is the type exhibited by 40 μm×2 μm samples. An example is shown in fig.6.2. The sample is tri21 (Py(50)/Nb(18)/Py(20)). A second type of behavior is shown by 40 μm×1 μm and 80 μm×1 μm samples. An example is given in fig.6.3 (sample tri23 short, Py(50)/Nb(20)/Py(20)). For both types we see two large blocks instead of four sharp peaks. For the first type they are closer to each other and less sharp defined than for the second type. One of the peaks has a more pointlike appearance. It is difficult to recognize the switching fields of the separate Py layers in these samples.

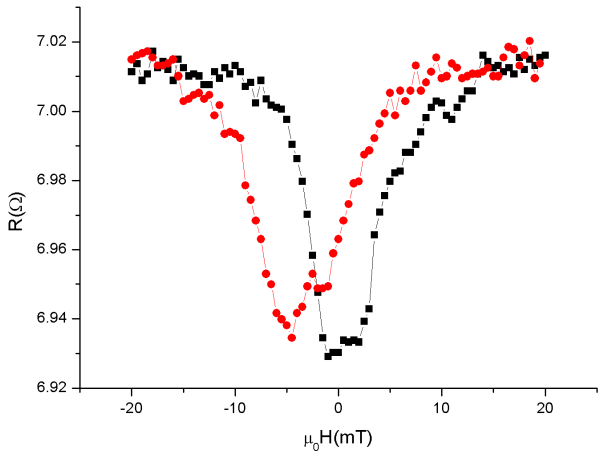

Figure 6.2: *The AMR effect in a 40×2 μm sample. This is an example of first type behavior. The sample shows 2 blocks close to each other. It is not possible to recognize the switching fields of the bilayers.*

The second type type has clear, well separated blocks. The switching field of the 20 nm Py layer is clearly distinguishable, and we expect the other jump to coincide with switching of the 50 nm layer. Also in this sample one of the blocks is a bit pointlike while the other is a real block.
We have also made large optically made structures to loose any lateral size effects. They are very large (width 20 or 200 μm) and they have no blocks as can be seen in fig.6.4 (sample tri30 large). The switching fields are very low (<5 mT) because in these large structures the layers can switch more easily. It is not entirely clear if the AMR signal is caused by one of the layers, the other layer switching

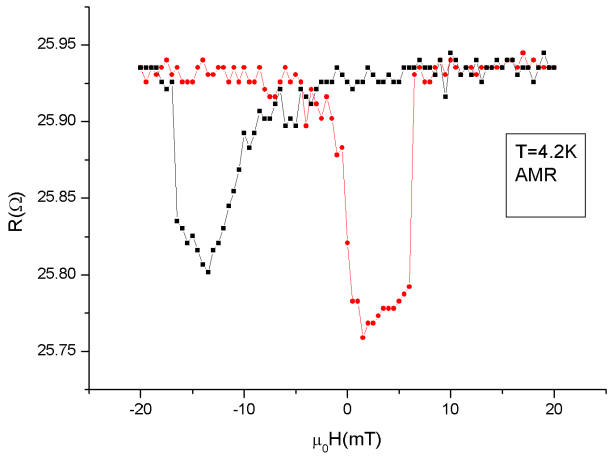

Figure 6.3: *The AMR effect in a 40×1 μm sample. This is an example of second type behavior. The sample shows 2 blocks further apart than in the sample in fig.6.2. In this sample the switching of one of the layers is clearly visible at 7.5 mT and -17.5 mT.*

invisibly fast or that both layers switch at the same time. It is impossible to see if there are two or four peaks. The behavior of these samples shows that the lateral dimensions are important for the determination of H_c and the switching behavior.

The graphs of AMR types one and two usually show some offset. The curves are shifted up to 5.0 mT in the positive or negative direction. Sometimes this can be caused by the remanent field of the magnet, especially if the samples are measured in the PPMS. But also samples measured in the ^{3}He cryostat show this effect. The ^{3}He cryostat has a very small magnet, the highest field we can obtain is just 50 mT and it seems improbable that such a magnet can cause 2.5 mT offset. The samples tri30-tri34 do not have an offset. This may be due to changes in the sample preparation. The origin of the asymmetry could be due to the presence of an oxidized Py layer, which acts as an antiferromagnet, and therefore an exchange bias, a not fully magnetized sample or the presence of spatially non-symmetric pin centers for domain walls.
For some particular samples we have seen a change of direction of the asymmetry (offset and/or differently shaped blocks) after warming the sample to room temperature and cooling down again. See the example of sample tri23 short in fig.6.5. This sample was measured in the ^{3}He cryostat (AMR1) then warmed to room temperature and again cooled down (the reason for doing this was an empty He vessel). After doing this the measurement was repeated (AMR2). The result looked completely different but this was solved by interchanging the + and

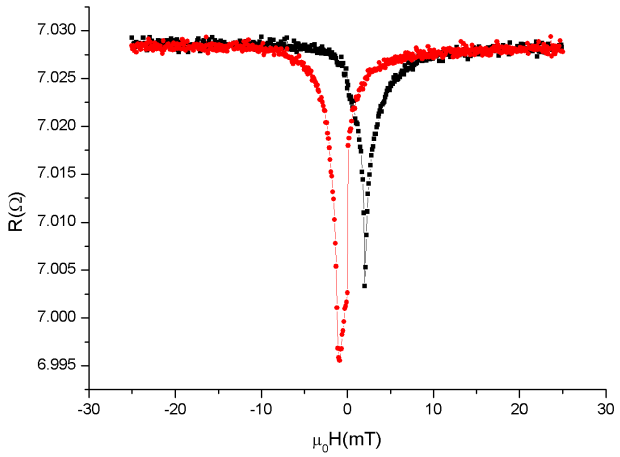

Figure 6.4: *The AMR effect in a optically structured sample (tri30 large, width=200μm). The curve has two peaks, apparently both layers switch at almost the same field or one of the layers is not visible.*

- signs of the field (AMR2 mirrored). This observation suggests the presence of a layer which causes exchange bias, probably an antiferromagnet with a Néel temperature between 10 K and 300 K. When the sample is cooled down, the exchange bias points in a certain direction and can not change direction until it warmed to room temperature.
It is important to know that the AMR measurement measures only the 10 μm in the middle of the strip. The other parts of the strip we do not measure. It is possible that the domain configuration in those parts and therefore the resistance in those parts changes without changing the resistance in the measured part. Therefore a non-changing AMR signal does not mean that the domain configuration is not changing.

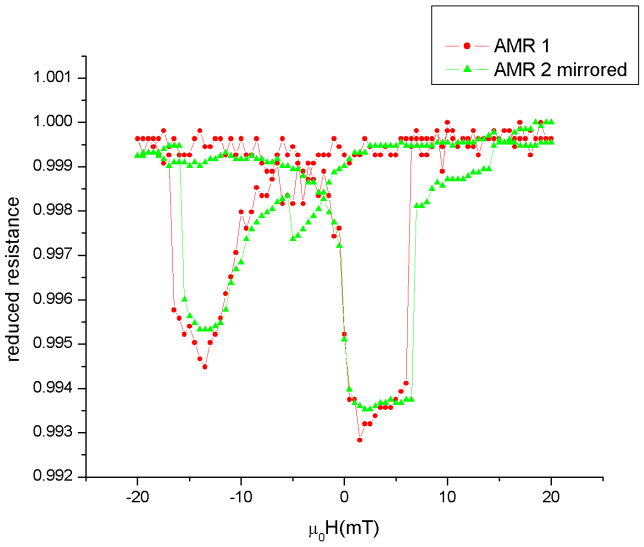

Figure 6.5: *The AMR effect before (AMR1) and after (AMR2) warming and cooling down again. AMR2 has changed the direction of the asymmetry with respect to field.*

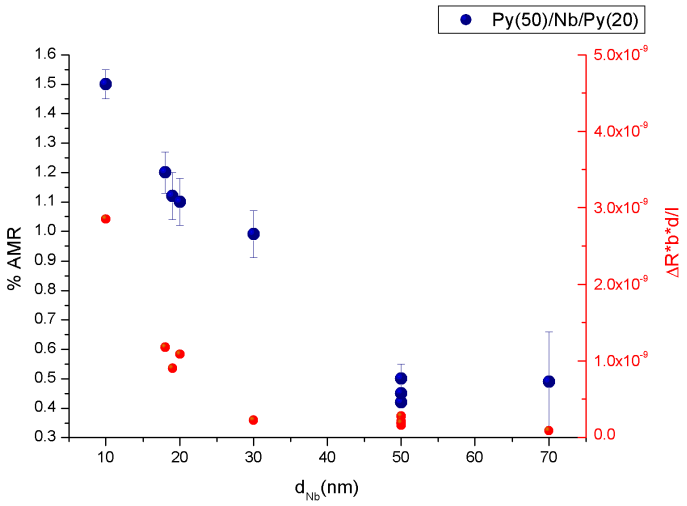

Figure 6.6: *(left axis) AMR percentage vs. Nb thickness (right axis) AMR resistance difference per unit volume Py vs. Nb thickness. This shows that in case of a 50 nm Nb trilayer the dimensions are not important with respect to AMR. The amount of AMR is the same for all dimensions. The 10 Nb data point is a bilayer with 20 nm Py which fits exactly where we expect a 10 nm Nb trilayer to be. The other bilayer with 50 nm Py shows no AMR.*

6.2 AMR vs. Nb thickness

The AMR percentage depends on the thickness of the Nb layer. In fig.6.6 (left side) the AMR percentage is given as function of Nb thickness. The sample with 10 nm Nb is not a trilayer but a bilayer with 20 nm Py. There are several samples with 50 nm Nb. They differ only in dimensions and direction of the easy axis. The sample dimensions are: one sample 2.5 mm×200 μm, one sample 1 mm×20 μm and three samples 40 μm×1 μm, of which two samples are structured under an angle of 45 ° with respect to the easy axis. All 50 nm samples have more or less the same % AMR. The right side of the same figure gives the resistance difference caused by AMR per unit volume Py. The 50 nm samples all give almost the same result. This is surprising because the samples have different dimensions, the small samples are nearly single domain structures and the large samples have many domains. The shapes of the AMR curves are also very different. The relative amount of magnetization perpendicular to the current direction however seems to be almost equal regardless of the sample dimensions.
The bilayer with 10 nm Nb was supposed to fit more at 20 nm Nb thickness, because it is basically a 20 nm trilayer cut in half. It is more like a 10 nm trilayer as the Nb thickness actually is. It seems that the amount of AMR of a s/Nb(10)/Py(20) bilayer and a s/Py(50)/Nb(10)/Py(20) trilayer is the same (but the shapes are completely different) and this suggests that the 50 nm Py layer does not have any influence on the size of the AMR signal. But the layer does definitely influence the shape of the AMR signal.

6.3 T_c vs. Nb thickness

The T_c of samples with different Nb thicknesses was measured. In this way it was possible to determine the critical thickness of this system and hence which are useful to measure RH curves. The results are given in fig.6.7. The measurements were all done in a field such that the ferromagnetic layers were certainly saturated in one direction (μ_0H=20 or 50 mT).
As can be seen, T_c decreases with decreasing thickness. The decrease is faster with decreasing thickness. Below a certain thickness the sample can not be superconducting anymore. This thickness is the critical thickness and here it is somewhere between 17.0 and 18.0 nm. The reason for this is that the Nb layer needs at least 2-3 ξ_0 to become superconducting, where $\xi_0 = \sqrt{\frac{\hbar D}{2\pi k_b T_c}}$. It can not be much less, because ξ is the length the sample needs to build up its full gap. The gap has its minimum at the interfaces and reaches its maximum value between the two interfaces. Therefore the sample needs at least 2-3 ξ. In that case ξ_0 of these samples is about 6-9 nm, which is reasonable because it is accordance with other estimates.
Two examples of RT measurements are given in fig.6.8 for samples with 20 and

50 nm Nb. The thinnest sample has the broadest transition. This is the case for all samples as can be seen in fig.6.9.

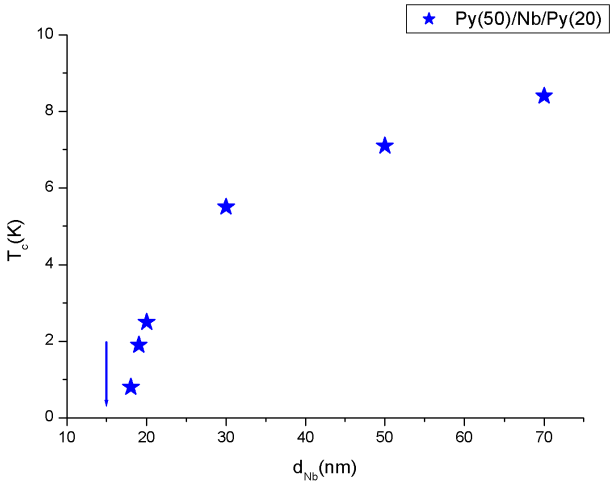

Figure 6.7: *T_c as function of Nb thickness in the trilayer s/Py(50)/Nb/Py(20). The critical thickness of this sample is around 18 nm.*

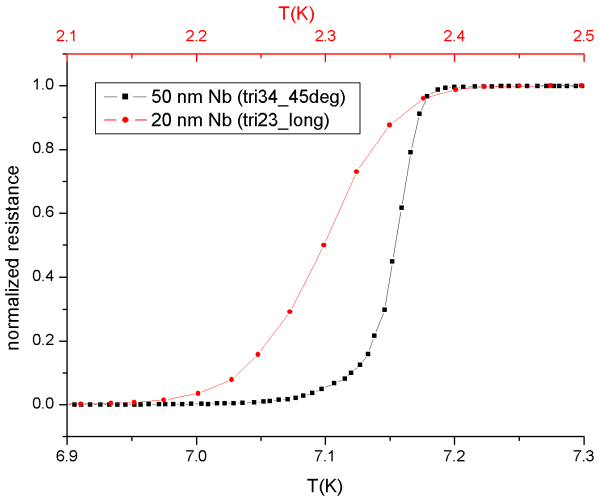

Figure 6.8: *The transition is broader if the sample is thinner as can be seen from these two samples with 20 and 50 nm Nb.*

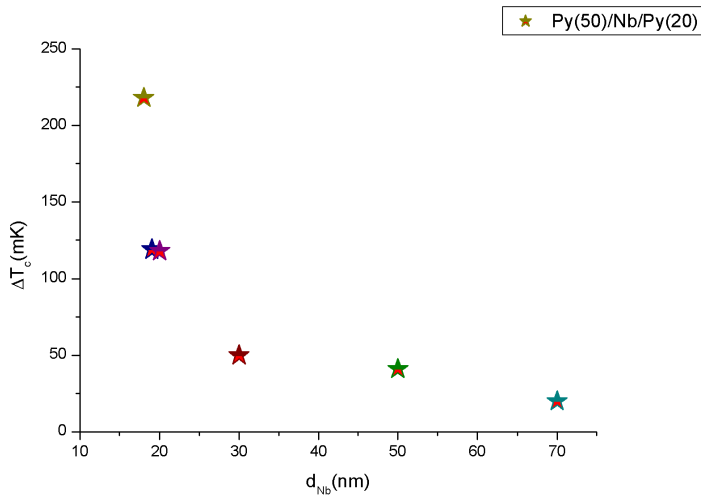

Figure 6.9: *The transition width as function of Nb thickness.*

6.4 H-dependence of RT curves

If $T_c^P \neq T_c^{AP}$, we can expect that the RT curves are non-identical as well. We measure RT as function of H to examine this behavior.
In fig.6.10 the result is shown for a sample with 19 nm Nb (tri22). The field started at μ_0H=-20 mT and was increased to 0 mT and again increased to 10 mT. We expect that we start in a P-state, then go to an AP-state and end in a P-state. The T_c is lowest if μ_0H=0 and 5 mT and highest if μ_0H= -20, -10 and 10 mT, and in between if μ_0H=-5 mT. The minus sign denotes the direction of the field. The sample was saturated at -20 mT. The fields where the T_c is high are supposed to cause a parallel configuration and the low T_c's are connected to an antiparallel configuration. For weak limit CuNi a shift in RT's was found [3] of about 10 mK at a T_c^{AP}=2.8 K and $T_c^{AP} > T_c^P$. For our sample the transition towards superconductivity seems to start at the same point for all fields but the RT curves broaden out for the non-P states and $T_c^{AP} < T_c^P$.

Fig.6.11 shows tri23 short, with 20 nm Nb. The measurement shows clearly the difference between the measurements with different fields. This is the sample which shows the biggest difference between T_c^{AP} and T_c^P. The difference is 95 mK at T_c (halfway the transition). The T_c not only broadens but is also shifted.

6.5 RH curves in the transition

Knowing the switching fields from AMR measurements, we now investigate how the spin switch behaves in the normal to superconducting state transition. Here

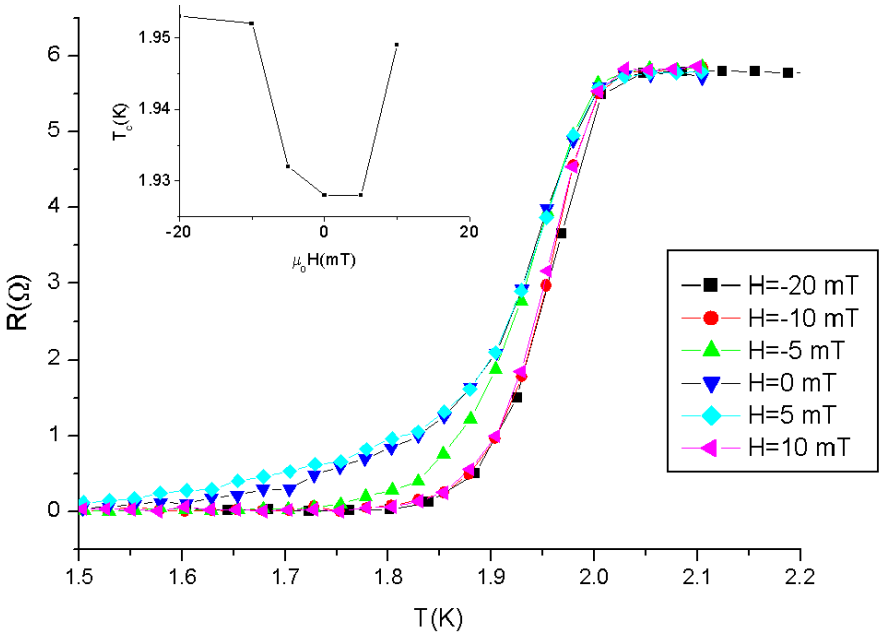

Figure 6.10: *a s/Py(50)/Nb(19)/Py(20) sample. The dimensions are 2×40 μm. RT was measured in several fields. It shows clearly the dependence on field. The inset shows the dependence of T_c on field. (T_c was measured halfway the transition at ±3 Ω)*

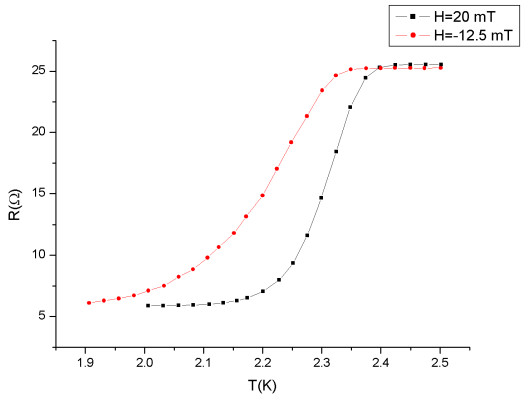

Figure 6.11: *A sample with 20 nm Nb. The difference between the two curves is clearly visible.*

Δ starts to develop, mostly shortcutting all resistive parts like Py layers. We now measure V_{Nb} instead of V_{Py} as in the AMR measurements. The resistance in these measurements is mainly due to inhomogeneous parts of Δ, thus to properties of

the Nb layer.

6.5.1 General behavior

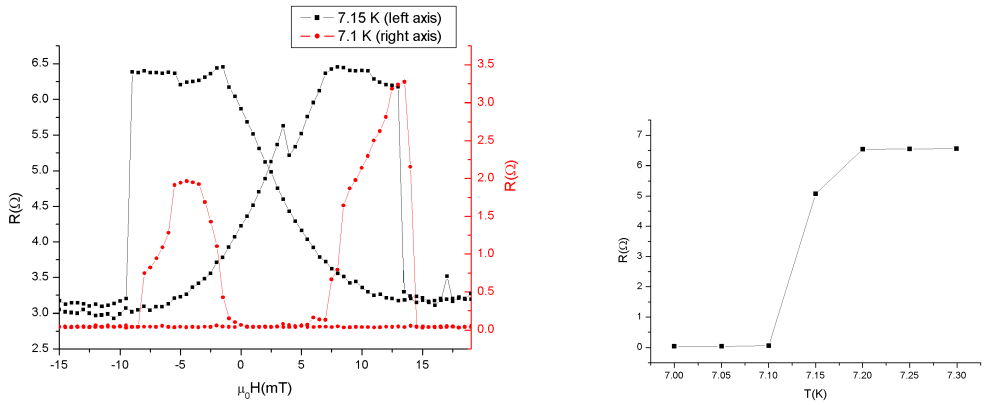

Figure 6.12: *Resistance as function of field for a sample with 50 nm Nb (tri16-L). Also shown is the RT of the same sample.*

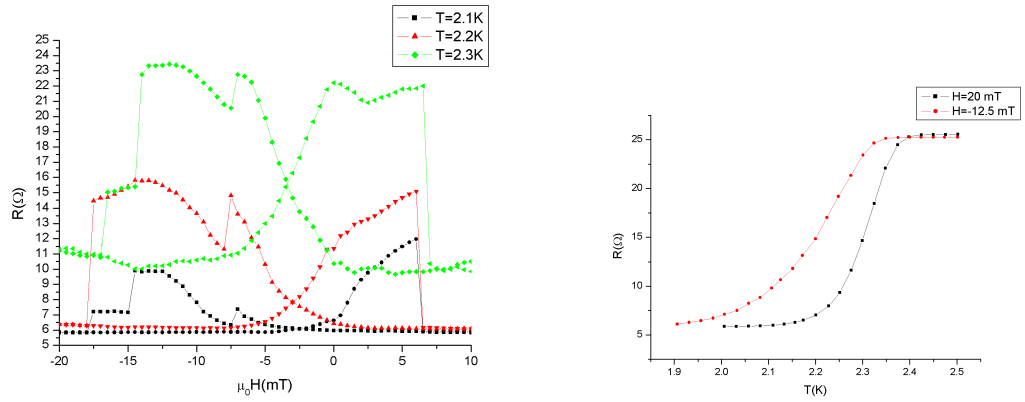

Figure 6.13: *Resistance as function of field for a sample with 20 nm Nb (tri23 short). Also shown is the RT of the same sample. (Note that the sample has a shortcut somewhere, the resistance below T_c is about 5 Ω.)*

We measured samples in the PPMS, in the ^{3}He cryostat and in the ^{4}He cryostat. Sample tri16-L in fig.6.12 was measured in the PPMS. Because the PPMS can only measure above 2 K and we wanted to measure at lower temperatures, we measured the next samples in the ^{3}He cryostat, for example sample tri23 short in fig.6.13. The last samples were measured above 2 K but because the PPMS did

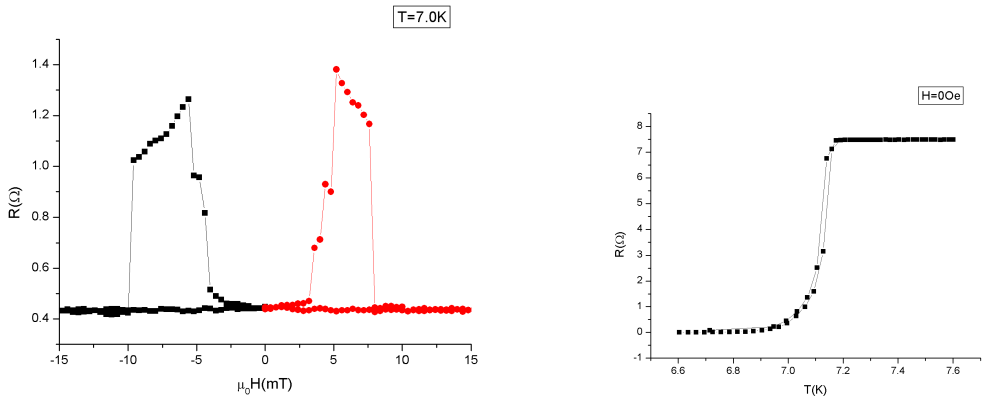

Figure 6.14: *Resistance as function of field for a sample with 50 nm Nb (tri34 0°). Also shown is the RT of the same sample.*

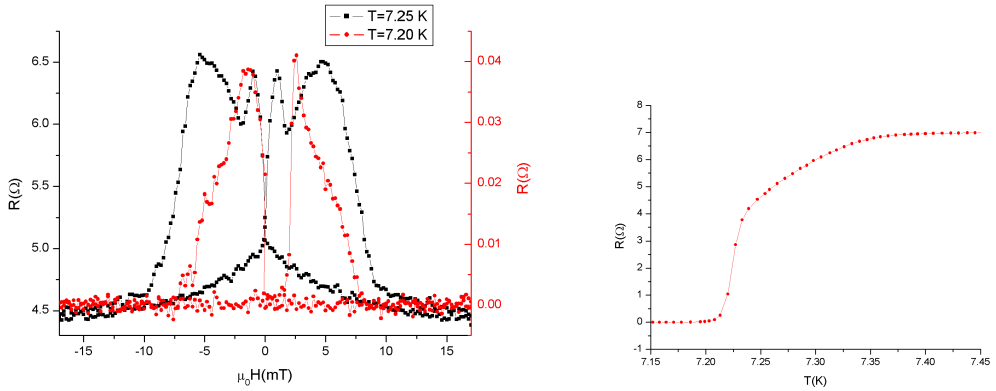

Figure 6.15: *Resistance as function of field for a sample with 50 nm Nb (tri30 large). This is a large optically structured sample. Also shown is the RT of the same sample.*

not have the desired temperature and magnet control, we measured them in the ^{4}He cryostat where the magnetic field steps are much smaller. Sample tri34 0° was measured in this way (fig.6.14). Fig.6.15 shows a large sample (2.5 mm×200 μm) measured in the same cryostat.
In general the resistance increases where we suppose the Py layers are antiparallel or otherwise non-parallel. There they make a block with usually a dip in the middle of the block. In most samples there is a sharp decrease in resistance at ±10 mT, very large samples do this at a lower field. Then the switch is also less sharp. At lower T the blocks are narrower, because then the gap is more developed are less influenced by the Py layers.

6.5.2 Measurement at higher field

To determine if the increase in resistance is caused by the direct effect of the external field or an antiparallel state it is possible to check at which higher field the resistance is as high as in the assumed antiparallel state. If this field is very low it is possible that the superconducting properties are suppressed by the external field or the field from a domain wall in the Py layers penetrating the superconductor. The external field needed to increase the resistance with the same amount as the 'antiparallel state' does, is about 150 mT (an example of a measurement is shown in fig.6.16, there the external field to get the required resistance increase is a bit higher, almost 190 mT.). This is a much higher field than we use to switch the Py layers and therefore the results we see are caused by the ferromagnets and not the external field. From this measurement it is not possible to know with certainty if the resistance increase is caused by an AP state or stray fields penetrating the superconductor. But if the stray fields are responsible, they should cause a field of at least 150 mT in the superconductor. The resistance then increases only in the neighborhood of a domain wall, so the field should actually be higher than this value to cause the same resistance increase.

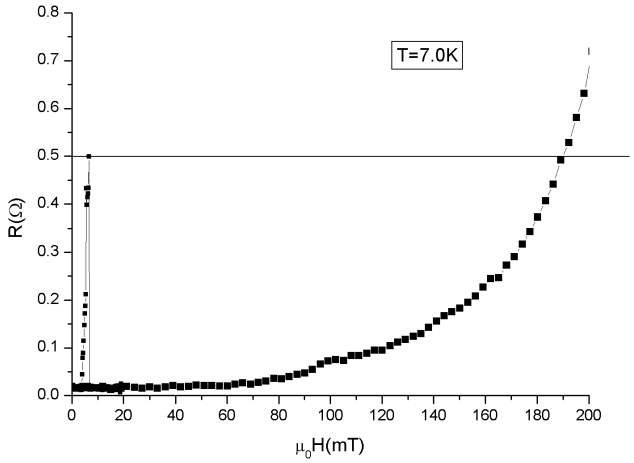

Figure 6.16: *A measurement at higher fields. The sample is tri34 45°. This shows that almost 190 mT was needed to increase the resistance the same amount as the antiparallel state did.*

6.5.3 Connecting RH to AMR

The similarities between RH(T>T_c) and RH(T<T_c) become more striking when we compare them directly. This is done for sample tri23 short in fig.6.17. The measurements in the transition have blocks at the same fields as the AMR measurements have dips. From this measurements and other measurements in the ^{3}He cryostat we see that saturation is very important. Because the magnet of the ^{3}He cryostat is very small, it is difficult to saturate the sample well. If the sample is not well saturated, we see switching in multiple steps. We want to do a careful measurement with different saturation fields to see the dependence on saturation field.

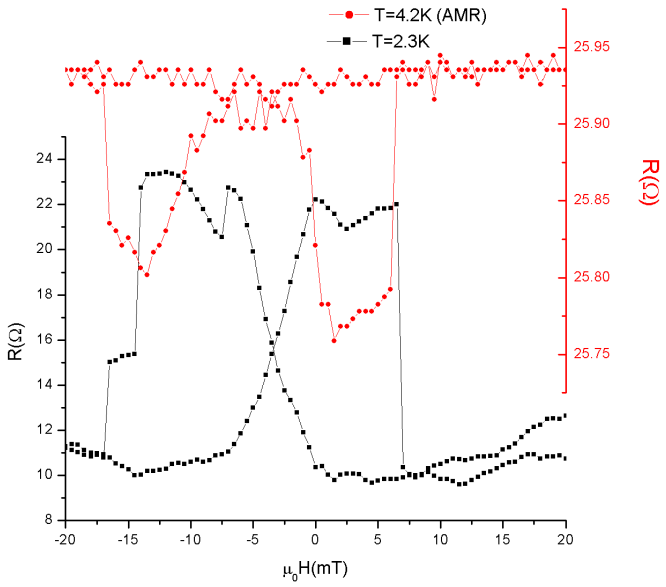

Figure 6.17: *Resistance as function of field, above and in the transition. The sample makes blocks in the transition where the AMR shows dips. The sample is tri23 short.*

6.5.4 AMR shape and saturation

The shape of the AMR curve also depends on the way the sample was saturated and on previous measurements. In fig.6.18 a series of AMR measurements is shown. The sample is tri34 0°. The measurement was as indicated in the figure. We see large dips which begin more or less at the same field for every measurement (at the left side at -4.1 mT and -3.1 mT and at the right side at 4.5 mT and 3.4 mT). They switch in multiple steps, switches are visible at -13.9 mT, -13.0

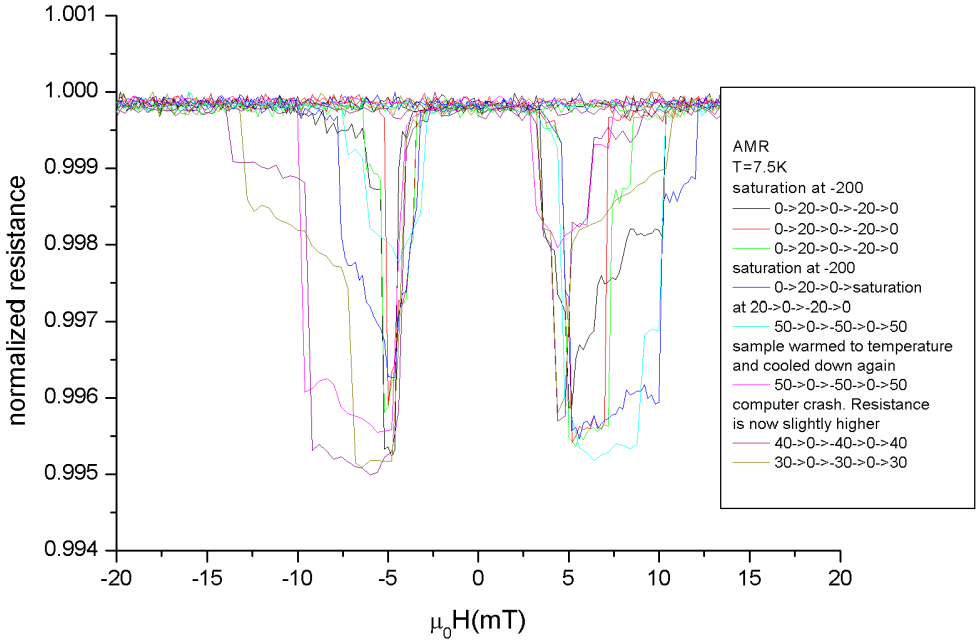

Figure 6.18: *8 AMR measurements under different conditions. Indicated in the legend are the external fields at which the measurement was started and ended (in mT). They give rise to different domain states and cause different switching fields. All blocks begin at the same field. The sample is tri34 0°*

mT, -10.0 mT, -7.6 mT, -6.3 mT and -5.2 mT at the left side and at 12.0 mT, 10.1 mT, 8.5 mT, 7.2 mT, 6.2 mT and 5.2 mT. Between the switches plateaus are visible at 0.995, 0.996, 0.998 and 0.999 of the normalized resistance and an additional one at the right side at 0.997. The plateaus indicate stable domain configurations. The shape of the AMR curve depends on the way the sample was saturated and on previous measurements. Each measurement has a small and a large dip. The first measurements have the large dip at the right side and the small dip at the left side but this is reversed after warming the sample to room temperature.

Similar measurements as the last three AMR measurements were performed in the transition. They are given in fig.6.19 together with the AMR. The measurements in the transition exactly follow the shape of the AMR measurements, especially at the left side of the figure. The same plateaus and switches as in the AMR measurement are present in the transition. The switches in the measurements in and above the transition are coupled. As shown in fig.6.20 this is not the case in a large optically structured sample (sample tri30 large). The large struc-

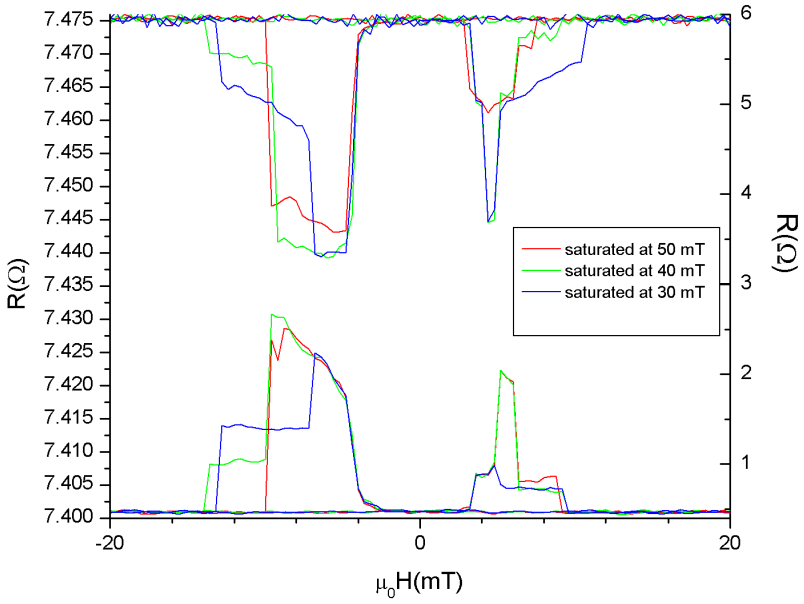

Figure 6.19: *AMR combined with measurements in the transition. The saturation conditions are the same for both measurements. The measurement in the transition exactly follows the AMR shape. The sample is tri34 0°*

ture has larger and broader blocks than AMR dips. The switches are not at the same fields. This can mean that in a small strip the switching both in normal and superconducting state is governed by shape anisotropy. In a large sample there is no shape anisotropy and the gap in the superconductor completely changes the switching fields of the Py layers. They become higher, so apparently the domain walls are pinned. In the normal state there is no gap which can influence the switching and then the layers switch faster.

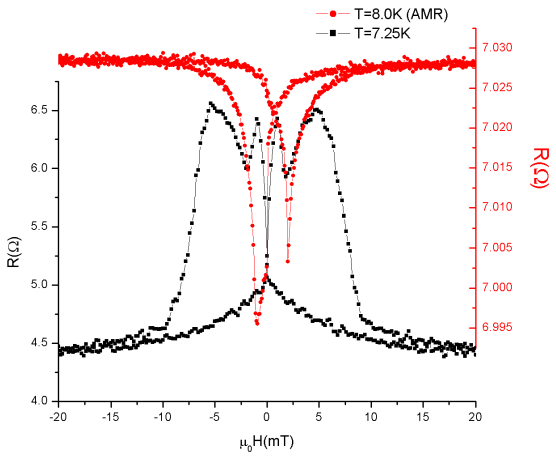

Figure 6.20: *Resistance as function of field, above and in the transition. The AMR has narrow dips while in the transition broader and more block like features appear. This is sample tri30 large*

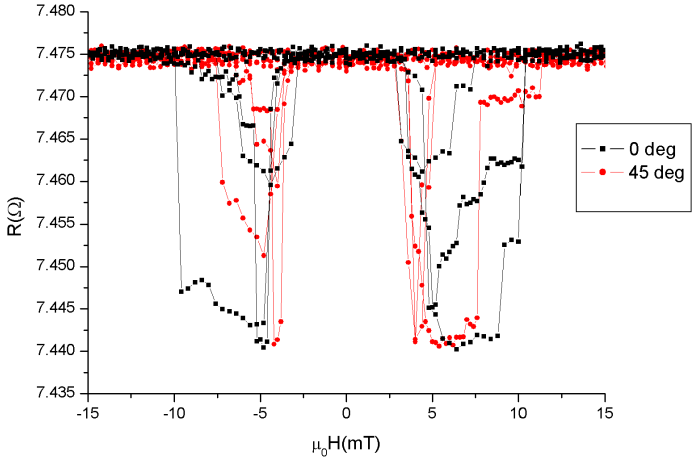

Figure 6.21: *Two samples with different orientations of the easy axis. The 45° sample was structured with a 45° angle with respect to the supposed easy axis. This sample seems to switch at lower fields than the 0° sample, structured along the easy axis. The samples are tri34 0° and tri34 45°*

6.5.5 AMR shape and easy axis

All these samples are supposed to have the easy axis aligned along the strip. To see if it is really crucial to have the easy axis in that direction or that the switching is entirely governed by shape anisotropy one sample (tri34) was made with two strips plus contact pads, one normal strip and the other strip under an 45 ° angle with respect to the supposed easy axis. Both strips have the same dimensions. They are measured with the strips parallel to the field. The AMR results are shown in fig.6.21. For both three measurements are shown, saturated in the same way (one time saturated at -200 mT and measured from -20 mT to +20 mT and reverse, two times measured from +50 mT to -50 mT and reverse without saturation). The AMR percentage is for both samples about 0.5%. The AMR dips begin at the same field but the 45 ° sample seems to switch back at a lower field, the dips are narrower. Although the measurement is not entirely conclusive, this seems to tell us that the direction of the easy axis influences the domain states the sample can enter. The direction of the easy axis causes the sample to enter and leave certain domain states more easily.

6.6 IV's

We also measured IV's to see if the resistance increase in the transition is caused by flux flow. IV's are measured for sample tri23 (20 nm Nb). The measurements as function of temperature are measured for a 80 μm long sample, the others for a 40 μm long sample. The IV's are reasonable symmetric. In fig.6.22 some IV's are given as function of temperature. This can be used to determine the T_c of the sample, because when it is a straight line it means that it is not superconducting anymore. The only problem is that it is very difficult to see if it is straight. It is better to use the derivative, dV/dI. This can be measured at the same time as the IV and is given in fig.6.23.

We can use this data to determine I_c(T) and from the temperature dependence the possibility that these I_c's are caused by flux flow or by depairing currents. If it is depairing current $I_c \propto (1 - T/T_c)^{3/2}$. We want to see if this temperature dependency is compatible with the data. The critical current is taken to be at the peak of the curves in fig.6.23, which is not entirely true but easiest to measure and the error is not too large. The result is given in fig.6.24 where we omitted the point at 2.5 K because that is already above the transition. The fitting curve gives a value for T_c and a constant which is not important at this moment. The fitted T_c is 2.8 K which is about 0.4 K higher than the measured one. The error can be caused by the assumption that the order parameter is constant in the whole S layer which is certainly not true. Another possibility is that the F layers cause such changes in the S layer that the theory is not able to handle them.

It is also possible to measure IV's as function of field. We expect that the

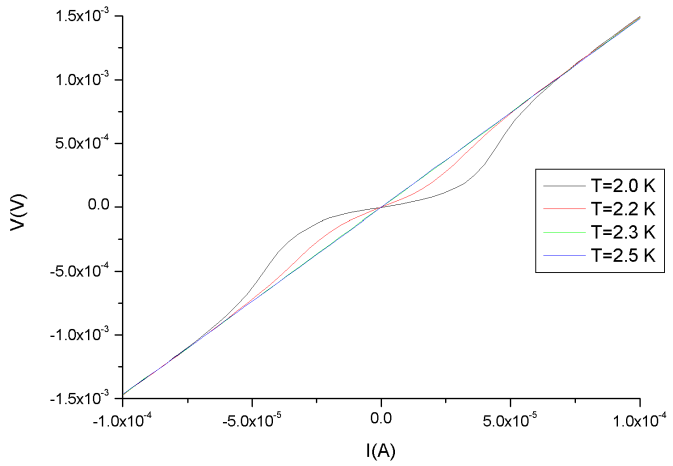

Figure 6.22: *IV curve for sample tri23 long.* $\mu_0 H$*=20 mT*

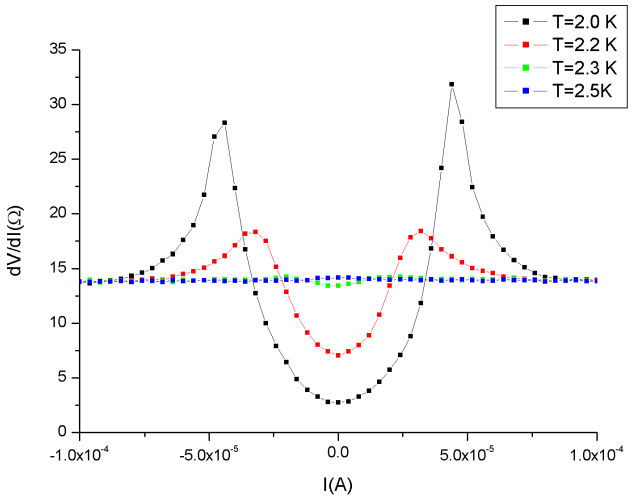

Figure 6.23: *dV/dI vs. I curve for sample tri23 long.* $\mu_0 H$*=20 mT. The temperature at which the gap starts to develop (here between 2.3 K and 2.5 K) is* T_c*.*

gap becomes wider in the parallel configuration and then the IV deviates from a straight line. The results are shown in fig.6.25-6.28 for two different temperatures together with a RH measurement at the same temperature (be aware that the sample has a shortcut and that the resistance below T_c is about 5 Ω). The fields at which the IV's are measured are indicated with arrows. The sample was

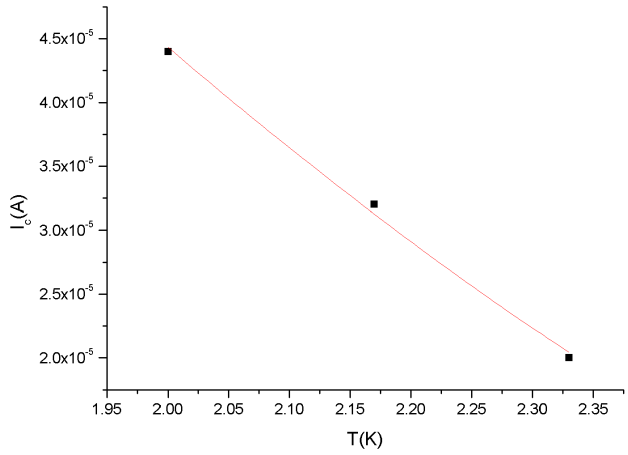

Figure 6.24: *I_c vs. T as taken from fig.6.23, with fit to theory.*

first measured at 2.1 K (fig.6.25 and 6.26). The broadest curve in fig.6.25 is the one with μ_0H=16 mT(parallel configuration). The μ_0H=12.5 mT curve has the smallest gap and is apparently at the top of the block. The behavior of all curves is essentially the same. There is no change in behavior if one goes from parallel to non-parallel state and this makes flux flow less probable. We measured this sample at I=10 μA and there the behavior is completely regular.

The same sample was measured at a lower temperature (1.8 K). The gaps are now wider. Around 0 A the 18 mT curve is now completely flat. The curve maybe looks like those connected to flux flow but at this field the resistance is lowest (see fig.6.28) and the other curves where there can be flux flow because the resistance is higher, are not flat around 0 A. The 10 mT curve shows strange bumps at higher currents, which are also vaguely visible in the 18 mT and 4 mT curve. Their origin is unknown.

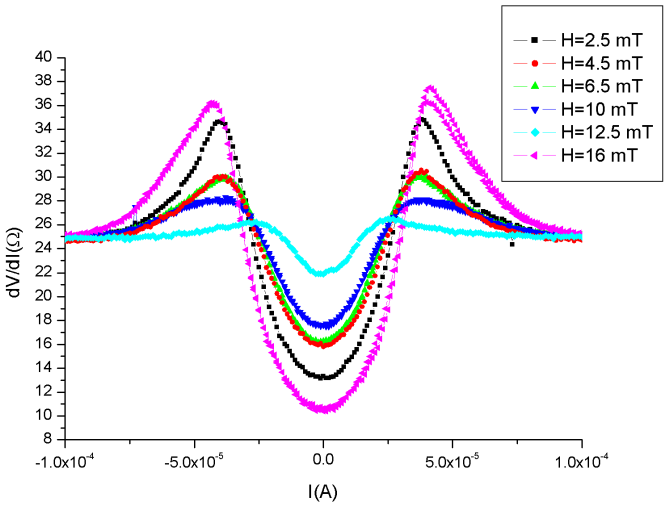

Figure 6.25: *dV/dI at T=2.1 K. The sample was saturated at $\mu_0 H$=-20 mT. The gap width shows large variation with applied field. It becomes wider if the field causes a lower resistance in the RH measurement. The RH measurement at the same temperature is shown in fig.6.26.*

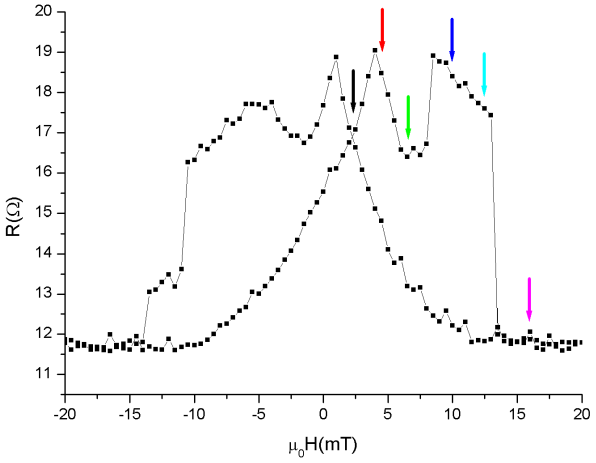

Figure 6.26: *RH at T=2.1 K. The applied fields used in the dV/dI measurement are indicated with arrows.*

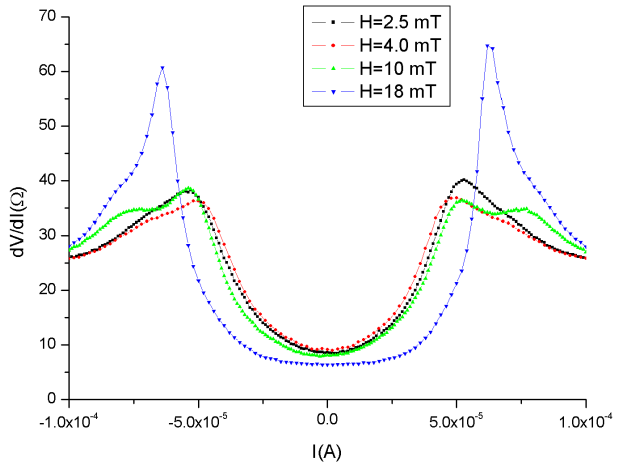

Figure 6.27: *dV/dI at T=1.8 K. The sample was saturated at $\mu_0 H$=-20 mT. The gaps are now wider than at 2.1 K. The 18 mT curve has a flat part around 0 A. At higher currents there are strange bumps visible of unknown origin.*

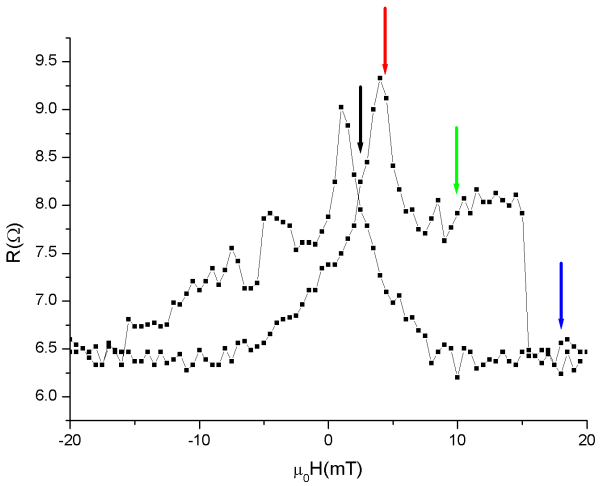

Figure 6.28: *RH at T=1.8 K. The applied fields used in the dV/dI measurement are indicated with arrows.*

Chapter 7

Discussion and conclusion

Now we can come back to the question of whether the stray fields of the domain walls in a domain state are responsible for the resistance difference between P and non-P states or that we have an effect of the P and AP states. We will argue below that it is very unlikely that the domain walls are responsible and we believe that the mechanism for this difference is the intrinsic nature of the P state to confine Cooper pairs. We believe that this confinement starts to dominate over the weak limit effects when the polarization has sufficiently reduced the Andreev reflection process.
Via IV we tried to exclude flux flow and via high field measurements we tried to rule out a global change in the superconducting gap. Field averaging of Cooper pairs near domain walls rules out itself since it should result in opposite sign.
High field measurements show that the applied field needed to increase the resistance the same amount as the non-P alignment of the Py layers does, is about 150 mT. This field is much higher than the fields we use. It shows that the external field does not influence the Nb layer much, it only switches the Py layers. It is possible that the field from a domain wall penetrating the superconductor locally exceeds 150 mT and causes resistance increase, but this can only happen exactly where a domain wall exists and it is unlikely that it increases the resistance of the whole strip.
The IV curves show no indication for flux flow. The critical current has a temperature dependency as expected in case of a depairing current. The dV/dI measurements show that the gaps become wider when the resistance decreases, as expected. The gaps become wider with decreasing temperature.
We think that this experimental evidence shows that the resistance increase is caused by P and AP states and not by domain walls which cause stray fields.

Conclusion We investigated the transport properties of a superconducting spin valve system. The superconductor Nb was sandwiched between two Py (permalloy=$Ni_{80}Fe_{20}$) layers. In particular we were interested in the difference in resistance between a parallel (P) and antiparallel (AP) alignment of the direction

of the exchange fields of the Py layers. Strips with typical dimension 40 μm$\times$1 μm were fabricated in order to induce high anisotropy which favors homogeneous magnetization in the F layers. The thickness of the F layers was fixed at 20 nm and 50 nm, resulting in coercive fields of 10 mT and 5 mT respectively, and so switching between P and AP states was possible. The Nb thickness was varied between 15 and 70 nm. In plane measurements were performed with applied external fields directed along the long side of the strip.

Anisotropic magnetoresistance (AMR) measurements on the spin valves in the normal state ($T>T_c$) shows that the manipulation of the direction of exchange fields is less ideal than expected. Based on the observed plateaus we conclude that domain states appear (a stable domain configuration in the Py layers which is neither fully P nor fully AP) rather than a fully AP state. This non-parallel (non-P) state brings along the effects of domain averaging and flux.

Transition temperature (T_c) measurements versus Nb thickness show the standard monotonous decrease of T_c with decreasing thickness with a critical thickness between 17 and 18 nm. The transition width increased from less than 50 mK at a thickness of 70 nm to over 200 mK at 18 nm thickness. Resistance measurements as function of temperature (RT measurements) for various applied fields around T_c show that the RT curves shift and broaden out to a lower value when the spin valve switches from P to non-P. A typical shift was of the order of 10 mK, the largest we found was 95 mK (for 20 nm Nb thickness).

AMR measurements on 40 μm$\times$1 μm strips show clear jumps and plateaus in the resistance, which become less well defined for dimensions of 40 μm$\times$2 μm and completely disappear for large 2.5 mm$\times$200 μm structures (instead we see the usual AMR behavior). Lowering the temperature to values inside the transition region enables us to investigate how the superconducting gap as influenced by the P and non-P states. We observe very similar behavior as in the AMR measurement, however, instead of rectangular dips we now see rectangular peaks. The peaks appear at the same applied fields as the AMR dips, and also the observed plateaus are matching.

We think that this resistance increase in the transition is caused by P and AP states of the F layers. IV measurements and high field measurements showed that it is unlikely that stray fields of domain walls are responsible for the resistance increase.

The shape of the AMR signal depends on the field used to saturate the sample. We found that in a sample with 50 nm Nb this has to be at least 50 mT. If it is less the sample will be not entirely saturated and parts of it will switch at a lower field than expected. This is the case in RH measurements above as well as in the transition. If the direction of the easy axis is not aligned with the strip, the sample can switch differently. In case of a 45 $^\circ$ angle the sample seems to switch earlier than a sample with 0 $^\circ$ angle.

Appendix A

How to make a trilayer sample

- clean substrates (7 mm×14 mm) with
  - demi-water
  - acetone
  - IPA
- Py/Nb/Py sputtering
  - use magnetic sample holder
  - tilt sample holder to align with sputter target (224 ° (horizontal state) for Nb, 179 ° for Py)
  - Nb sputter parameters: p_{Ar}=4.0 μbar, I=220 mA, V≈320 V, sputter rate =0.118 nm/s
  - Py sputter parameters: p_{Ar}=2.5 μbar, I=165 mA, V≈470 V, sputter rate = 0.203 nm/s
- spincoat resist (maN 2405) at 6000 rpm
- bake resist at 90 °C for 10 min.
- write strips using the SEM
  - 10 mm work distance, aperture 2
  - 100μm×100μm write field, zoom factor 600
  - beam current =0.1 nA, dose = 45 μC/cm^2
- develop in maD for 70 s followed by demi-water dip
- Ar etching
  - use N_2 cooling and rotating sample holder

  - use recipe 10 and $2.5 \cdot 10^{-4}$mbar Ar
  - etch rate: 0.33 nm/s (Py), 0.22 nm/s (Nb)
- 45 min. Acetone dip to remove remaining resist
- spincoat resist (PMGI SF5) at 4000 rpm
- bake resist at 200 °C for 60 min.
- spincoat resist (PMMA A4) at 4000 rpm
- bake resist at 160 °C for 30 min.
- write contacts (SEM)
  - 20 mm work distance, aperture 2
  - 3 mm×3 mm write field, zoom factor 20
  - beam current =10 nA, dose = 200 μC/cm^2
- develop in MIBK:IPA=1:3 for 35 s., followed by IPA dip
- develop in PMGI 101 for 5 min., followed by demi-water dip
- contact sputtering (ATC)
  - p_{Ar}=3 mTorr, Ar flow≈25 sccm
  - Ti target has to be presputtered for about 15 min (I=200 mA)
  - Ti sputter parameters: I=400 mA, 60 s.
  - Au sputter parameters: I=100 mA, 10 min.
- lift off in NMP (several hours)

Appendix B

List of measured samples

In the following table B.1 the dimensions and thicknesses of the layers are given for all samples that have been mentioned previously. From left to right are given: the sample number, the thickness of the bottom Py layer, the thickness of the Nb layer, the thickness of the top Py layer, the presence of a 2 nm thick Nb capping layer and the dimensions of the strip. The length of the tri30 samples was measured between the voltage contacts as the whole length is less well defined (it includes current contact pads).

sample ID	Py thickness (nm)	Nb thickness (nm)	Py thickness (nm)	Nb cap y/n	dimensions
bi20	-	10	20	n	40 μm×2 μm
bi50	50	10	-	n	40 μm×2 μm
tri16-L	50	50	20	n	40 μm×2 μm
tri17	50	70	20	n	40 μm×2 μm
tri18	50	30	20	n	40 μm×2 μm
tri19	50	15	20	n	40 μm×2 μm
tri21	50	18	20	n	40 μm×2 μm
tri22	50	19	20	n	40 μm×2 μm
tri23 long	50	20	20	n	80 μm×1 μm
tri23 short	50	20	20	n	40 μm×1 μm
tri30 small	50	50	20	n	1 mm×20 μm
tri30 large	50	50	20	n	2.5 mm×200 μm
tri32 45°	50	50	20	y	40 μm×1 μm
tri34 0°	50	50	20	y	40 μm×1 μm
tri34 45°	50	50	20	y	40 μm×1 μm

Table B.1: Thicknesses and dimensions of the measured samples.

Bibliography

[1] L.R. Tagirov, Phys. Rev. Lett. **83**, 2058 (1999)

[2] A.I. Buzdin, A.V. Vedyayev and N.V. Ryzhanova, Europhys. Lett. **48**, 686 (1999)

[3] J.Y. Gu et al., Phys. Rev. Lett. **89**, 267001 (2002)

[4] A.Yu. Rusanov, S. Habraken and J. Aarts, Phys. Rev. B **73**, 060505 (2006)

[5] D.Y. Petrovykh et al., Appl. Phys. Lett. **73**, 3459 (1998)

[6] M. Tinkham, Introduction to Superconductivity, Dover publications (2004)

[7] S. Blundell, Magnetism in Condensed Matter, Oxford University Press (2006)

[8] R.C. O'Handley, Modern Magnetic Materials, John Wiley & sons (2000)

[9] G.E. Blonder, M. Tinkham and T.M. Klapwijk, Phys. Rev. B **25**, 4515 (1982)

[10] E.A. Demler, G.B. Arnold and M.R. Beasley, Phys. Rev. B **55**, 15174 (1997)

[11] M.J.M. de Jong and C.W.J. Beenakker, Phys. Rev. B **74**, 1657 (1995)

[12] M. Flokstra, private communication